Journal of Materials Chemistry A

ROYAL SOCIETY OF CHEMISTRY

PAPER

View Article Online
View Journal | View Issue

Check for updates

Cite this: J. Mater. Chem. A, 2026, 14, 7779

Interface-directed synthesis of $CsPbBr_3$-based particles with water-ODE antisolvent systems

Saurabh Singh, *[a] Xiyu Wen[b] and Fuqian Yang [a]

All-inorganic lead halide perovskites, specifically $CsPbX_3$ (X = I, Cl, Br), have attracted significant attention over the past few years due to their immense potential in optoelectronic devices, such as liquid crystal displays (LCDs), light emitting diodes, photodetectors, and solar cells. Currently, most available synthesis techniques rely on high temperatures, inert environments, and toxic non-polar solvents, with limiting scalability and environmental compatibility. Herein, we present a facile, room-temperature, and partially green approach for synthesizing $CsPbBr_3$-based particles *via* a biphasic solvent system comprising non-polar octadecene (ODE) layered over deionized water. By simply tuning the volume ratio of DI water to ODE, we used interfacial engineering to modulate the formation and growth of $CsPbBr_3$-based particles. Pure water system without ODE yielded highly crystalline, phase-pure $CsPbBr_3$ of ~0.5 μm in size (BPPT0) with strong green photoluminescence at ~534 nm. A system with 1 : 1 of water to ODE favored the formation of small $CsPbBr_3$ particles of ~0.1 μm in size with trace amounts of Cs_4PbBr_6 impurity (SPPT1). The as-synthesized SPPT1 particles exhibited strong photoluminescence at ~524 nm and broader color gamut coverage of ~123% of NTSC 1953 and ~174% of sRGB when being incorporated in white emitting LCD backlight structures. Further, both BPPT0 and SPPT1 displayed excellent ambient stability. This work demonstrates interfacial solvent engineering as a powerful strategy for the synthesis of size-controlled perovskite under scalable and environmentally responsible conditions.

Received 13th September 2025
Accepted 20th January 2026

DOI: 10.1039/d5ta07491f

rsc.li/materials-a

Open Access Article. Published on 26 January 2026. Downloaded on 5/30/2026 3:48:49 AM.
This article is licensed under a Creative Commons Attribution 3.0 Unported Licence.

1 Introduction

All-inorganic lead halide perovskites of $CsPbX_3$ (X = Cl, Br, I) have emerged as a key player in developing photovoltaic devices such as LEDs (light emitting diodes), solar cells and photodetectors owing to their excellent opto-electronic properties namely high defect tolerance, remarkable thermal stability, fine emission bandwidth, high color purity *etc.*[1–7] However, realizing these materials in practical devices critically depends on the ability to fabricate high-quality, phase-pure, and morphologically uniform materials with minimal defects.[8–12]

Over the past few years, several synthesis techniques have been implemented to fabricate high-quality green emitting $CsPbBr_3$ particles with high crystallinity and notable optoelectronic performance. For instance, the standard hot-injection synthesis method enables high-quality $CsPbBr_3$ nanocrystal formation with tunable morphology and excellent optoelectronic properties, but typically requires elevated temperatures (140–300 °C) and strict inert conditions with controlled precursor injection, which complicate large-scale production.[13–16] Another widely adopted room-temperature synthesis route for $CsPbBr_3$ nanocrystals is ligand-assisted reprecipitation (LARP) method which offers simplicity and operation at ambient temperatures (<70 °C) with minimal equipment requirements, however, it still relies heavily on organic and toxic solvents (such as toluene and hexane) and lengthy ligand purification steps, and achieving reproducible quality at high yields remains challenging.[17–19]

The strong ionic behaviour of $CsPbBr_3$ perovskites further aggravates these limitations, making them highly unstable in the presence of moisture and polar solvents such as water, acetone, and ethanol *etc.*[20–23] Such exposure often leads to rapid phase transformation from $CsPbBr_3$ to non-radiative Cs_4PbBr_6 and/or the decomposition of $CsPbBr_3$.[24,25] Other synthesis approaches for $CsPbBr_3$ particles, such as solvothermal and microwave-assisted methods, have been shown to enhance crystallinity and accelerate reaction kinetics, however, these strategies often demand elevated temperatures, autogenous pressures, and specialized reactor setups, which often complicate the process control and pose challenges for large-area or high-throughput scale-up strategies.[26–28]

Tremendous efforts have been invested into understanding the degradation mechanism of $CsPbBr_3$ at atomistic scale in polar environments.[24,25,29] On contrary, several reports highlighted the correlation of moisture with enhanced optoelectronic behavior of perovskite materials including $CsPbBr_3$ with better crystallinity and lower surface defects.[30–33] A few water-assisted synthesis methods have recently emerged as

[a]Materials Program, Department of Chemical and Materials Engineering, University of Kentucky, Lexington, KY 40506, USA. E-mail: ssi303@uky.edu
[b]Center for Aluminium Technology, University of Kentucky, Lexington, KY 40506, USA

Open Access Article. Published on 26 January 2026. Downloaded on 5/30/2026 3:48:49 AM. This article is licensed under a Creative Commons Attribution 3.0 Unported Licence.

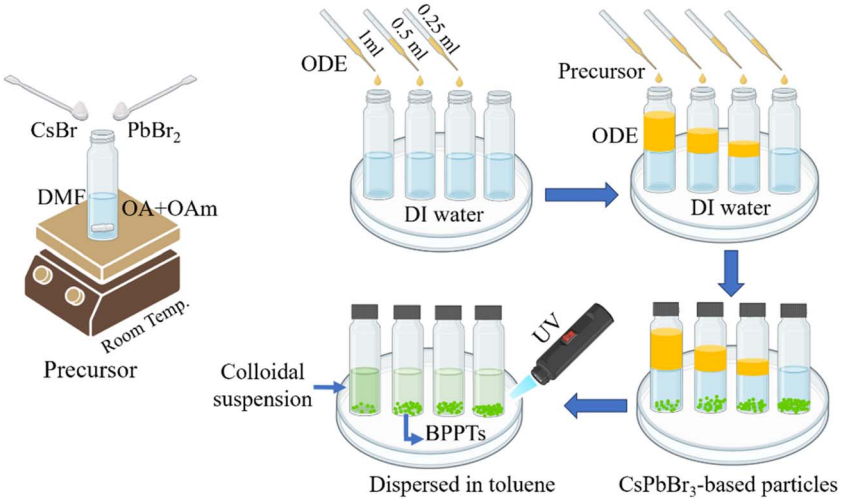

Fig. 1 Schematic of the synthesis route of $CsPbBr_3$-based particles.

promising alternatives to improve crystallinity, reduce toxicity, and modify band gap or consequently the luminescent behavior of the prepared perovskites.[34–40] For instance, Zhang, *et al.*[36] introduced small traces of water in toluene when synthesizing $CsPbBr_3$ particles using LARP method and reported the change in size, crystallinity and phase purity with different amounts of water introduced leading to red shift of PL (photoluminescence) peak and enhanced opto-electronic properties such as higher PLQY (quantum yield) and better stability.[36] However, such reports not only demand non-polar solvent environments during synthesis but also lack the mechanisms controlling nucleation and growth, phase purity, and size selectivity.

There are various approaches implemented to control the nucleation and growth kinetics of $CsPbBr_3$ such as solvothermal, sonication, mechanochemical and microwave irradiation.[41–44] These techniques utilize non-polar solvents such as benzyl ether (BE) and 1-octadecene (ODE) during the synthesis to achieve better control of crystallinity and morphology of perovskite particles including $CsPbBr_3$, owing to their non-polar behavior and high boiling point. Zamani, *et al.*[45] studied the effect of non-polar solvents on the growth of $CsPbBr_3$ particles and concluded that using BE in one-pot synthesis and microwave irradiation resulted in formation of highly crystalline nanoplates while using ODE resulted in formation of smaller crystallites owing to effective solvation of $PbBr_2$ in BE compared to ODE. However, such methods still rely on high temperatures, high energy radiations, inert atmosphere, complex synthesis *etc.*[45] Therefore, achieving a synthesis technique that balances phase selectivity, crystallinity, morphology, optical performance, and ambient stability while being simple, cost effective and environment friendly up to a certain degree, under benign and scalable conditions, remain elusive.

In this work, we report for the first time a facile and scalable synthesis route, as shown in Fig. 1, under ambient conditions for $CsPbBr_3$-based particles *via* a biphasic system with non-polar ODE over polar deionized (DI) water, achieving a unique interfacial environment to control the particle size, phase purity of as-obtained $CsPbBr_3$-based particles, without the need for inert environments, high-temperature injection, or ligand-intensive stabilization. As a result, this approach provides a fundamentally distinct and scalable processing framework that is more compatible with low-cost, environmentally benign, and potentially continuous manufacturing of $CsPbBr_3$-based optoelectronic materials. By tuning this polar-non polar solvent interface, we obtained large precipitates (BPPT0) of ~0.5 μm in size and small precipitates (SPPT1) of ~0.1 μm in size. The as-obtained $CsPbBr_3$-based particles exhibit distinct phase composition, impurity levels, PL behavior, ambient stability, and display color profiles.

2 Experimental details

2.1 Synthesis of $CsPbBr_3$-based particles

For the precursor preparation, CsBr (0.042 mmol) and $PbBr_2$ (0.042 mmol) were dissolved in 5 ml of *N*,*N*-dimethylformamide (DMF) containing 50 μl of oleylamine (OAm) and 187.5 μl of oleic acid (OA) at room temperature (~16 °C) under vigorous stirring for ~8 hours until a clear transparent solution is obtained as the "precursor" solution. Four different glass vials, pre-filled with 1 ml DI water each, were filled with different amounts of ODE (specifically, 1 ml, 0.5 ml, 0.25 ml, and 0 ml) to achieve volume ratios of $1 : x$ ($x = 1$, 0.5, 0.25, 0) for DI water to ODE, respectively. After two different immiscible layers were formed, the prepared precursor solution of 5 ml was poured into all four glass vials. Immediately, green emitting particles were formed at liquid–liquid and liquid–glass interfaces while most particles were observed on the bottom of the vials. These as-formed $CsPbBr_3$-based particles were extracted carefully and redispersed into 1 ml of toluene to separate bigger particles from the "colloidal" suspension.

2.2 Preparation of $CsPbBr_3$-based 'films'

Three different kinds of 'films' were produced on glass substrate from the $CsPbBr_3$-based particles, which were formed

 This journal is © The Royal Society of Chemistry 2026

Open Access Article. Published on 26 January 2026. Downloaded on 5/30/2026 3:48:49 AM. This article is licensed under a Creative Commons Attribution 3.0 Unported Licence.

with different ratios of DI water to ODE. Overall, 12 different films were fabricated and characterized.

2.2.1 Big precipitates (BPPTs) thin films. After extracting BPPTs from colloidal solution through natural sediment, they were deposited on clean glass substrate using a drop-caste method and were dried in open-air conditions for nearly 2 hours before characterization.

2.2.2 Small precipitates (SPPTs) thin films. The colloidal solutions after removing BPPTs were centrifuged at 8000 rpm for 5 min resulting in sediment of bigger particles on bottom. These particles were extracted carefully and were deposited on clean glass substrate *via* the drop-caste method and were dried in open-air for nearly 5–6 hours before characterization.

2.2.3 Supernatant (SNT) thin films. After centrifugating colloidal QDs and extracting SPPTs, 100 μl of the supernatant was deposited on clean glass substrate *via* the drop caste method and were dried in open-environmental conditions for 3–4 hours before characterization.

2.2.4 Red emissive phosphor film. A red EXPO marker pen was used to extract red ink. 100 μl of the ink was drop-casted on glass substrate, which was followed by open-air drying.

2.3 Materials characterization

The morphological and chemical compositional analyses were conducted on a scanning electron microscope (SEM) (JEOL JSM-5900lLV) equipped with an energy-dispersive X-ray spectroscope (EDS). The structural characterization of as-prepared $CsPbBr_3$ films was performed on an X-ray diffractometer (XRD) (Siemens D500) with CuKα radiation ($\lambda = 1.5406$ Å). The PL studies of the as-prepared $CsPbBr_3$ films were carried out using a spectrometer (Ocean optics, FLAME-S-VIS-NIR-ES, Ocean Optics, Orlando, FL, USA) with a UV excitation wavelength of 365 nm. The lifetime decay studies were conducted using a DeltaHub™ high throughput time correlated single photon counting (TCSPC) controller.

3 Results

Fig. 2a and b shows typical SEM images of BPPT0 (BPPT prepared using pure DI water) and SPPT1 (SPPT prepared using 1 : 1 ratio of DI water to ODE), respectively. Both the BPPT0 and SPPT1 exhibit cuboid-shaped morphologies in accord with the orthorhombic phase of $CsPbBr_3$. Fig. 2c and d shows the size distribution of the BPPT0 and SPPT1, respectively, which are derived from Fig. 2a and b. The average particle size of the BPPT0 is ~500 nm significantly bigger than ~100 nm of the SPPT1. The EDS spectral analysis, shown in Fig. S1a–d, demonstrated that the Cs : Pb : Br atomic ratios in both BPPT0 and SPPT1 are close to the 1 : 1 : 3 stoichiometry, consistent with $CsPbBr_3$ being the dominant phase in these samples.

Note that both the BPPT0 and SPPT1 exhibit high crystallinity compared to some previous works.[40] For instance, Xiang,

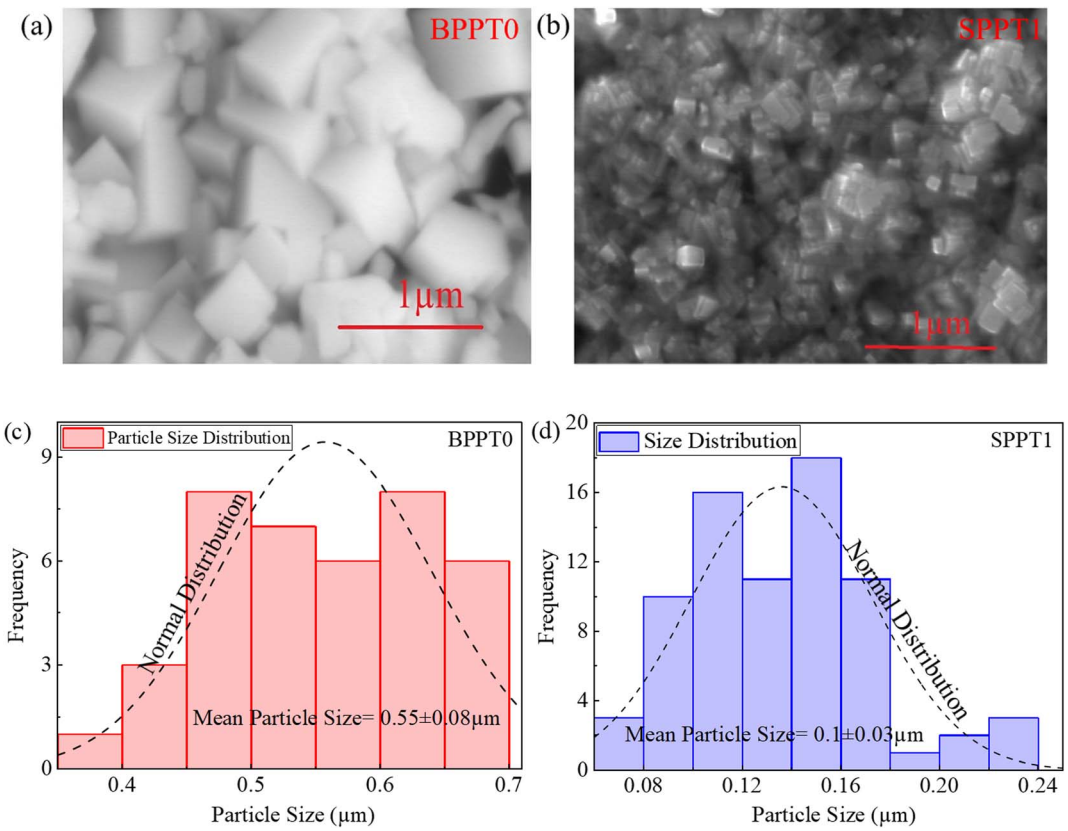

Fig. 2 (a and b) SEM images of BPPT0 and SPPT1, and (c and d) histograms depicting the size distribution of the BPPT0 and SPPT1 shown in a and b.

Open Access Article. Published on 26 January 2026. Downloaded on 5/30/2026 3:48:49 AM.
This article is licensed under a Creative Commons Attribution 3.0 Unported Licence.

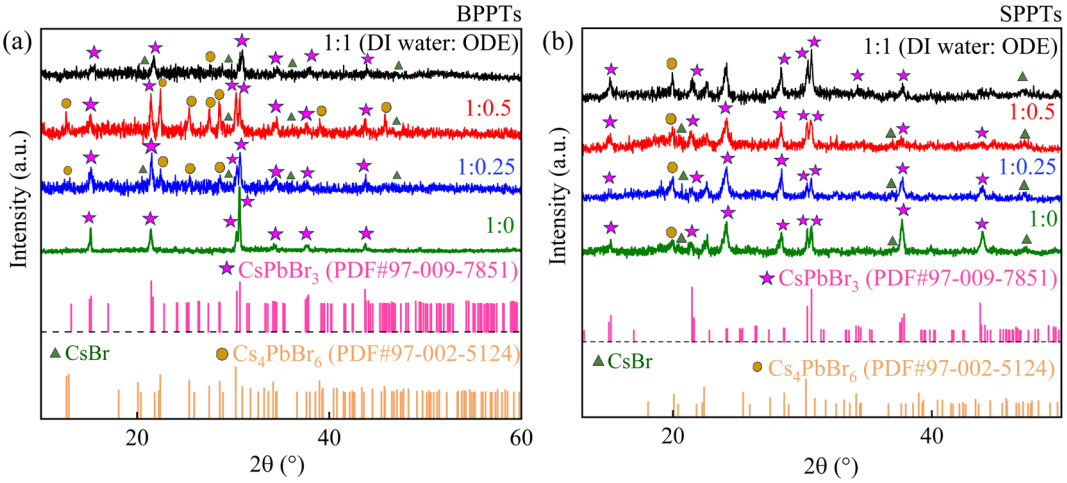

Fig. 3 (a) XRD pattern of $CsPbBr_3$-Cs_4PbBr_6 mixed-phase BPPTs, and (b) XRD spectra of $CsPbBr_3$-Cs_4PbBr_6 mixed-phase SPPTs with different molar ratios of water to ODE.

et al.[46] reported lower crystallinity (shown *via* SEM images) of the prepared $CsPbBr_3$ films with average particle size of ~0.47 μm *via* vacuum thermal evaporation.

Fig. 3a and b shows XRD spectra of the BPPTs and SPPTs synthesized with 4 different volume ratios of DI water to ODE. As evident from Fig. 3a, the BPPT sample prepared *via* pure DI water (DI water : ODE ratio of 1 : 0) exhibits only the characteristic reflections of orthorhombic $CsPbBr_3$ phase, with major peaks centered at 2θ ~15.2°, 21.4°, 30.3°, 30.6°, 34°, 37.7°, and 43.7° corresponding to (110), (112), (004), (220), (130), (132), and (224) planes (PDF#97-009-7851), indicating phase-pure $CsPbBr_3$ within the detection limit of XRD.

On contrary, all other BPPT samples prepared with 1 : 1, 1 : 0.5, and 1 : 0.25 ratios of DI water to ODE, showed additional diffraction peaks at 2θ ~12.6°, 22.4°, 25.4°, 27.5°, 28.6°, 38.9°, 45.8°, which are indexed to the (012), (300), (024), (131), (214), (324), (137) planes of hexagonal Cs_4PbBr_6 phase (PDF#97-002-5124), confirming the formation of $CsPbBr_3$-Cs_4PbBr_6 mixed-phase composites in these samples. Similar coexistence of dual phases is well reported in the literature.[47–49] Among these BPPTs (1 : 1, 1 : 0.5 and 1.0.25), the sample prepared with the ratio of 1 : 0.5 (DI water: ODE) exhibited the most intense peaks for secondary Cs_4PbBr_6 phase, suggesting preferential trap of Pb^{2+} ions at the water-ODE interface due to partially nonpolar environment and being consistent with the reports that partial nonpolar environments and excess CsBr favour the formation of Cs_4PbBr_6 phase.[50]

Similar $CsPbBr_3$-Cs_4PbBr_6 phase coexistence was observed in all SPPT samples prepared with 1 : 1, 1 : 0.5, 1 : 0.25, and 1 : 0 ratios of DI-water to ODE (Fig. 3b). Moreover, in all SPPT samples, orthorhombic $CsPbBr_3$ was identified as the dominant crystalline phase, while hexagonal Cs_4PbBr_6 was present only as a minor secondary phase, indicated by its low-angle reflections at ~20° and depicted in Fig. 3b. Using Bragg's law[51] and the XRD patterns (Fig. 3a and b), we calculated the interplanar spacing (d) of the orthorhombic $CsPbBr_3$ phase for all BPPT and SPPT samples using the characteristic peak centred around ~30.6°, corresponding to (220) crystallographic planes of orthorhombic $CsPbBr_3$. The mean interplanar spacing for the orthorhombic $CsPbBr_3$ reflections was found to be ~2.903 ± 0.012 Å for BPPT samples and 2.911 ± 0.003 Å for SPPT samples, indicating that variations in processing conditions did not induce any measurable distortion in the orthorhombic $CsPbBr_3$ lattice structure.

Fig. S2a–c in the SI presents optical images of 12 films deposited on glass substrates using BPPTs, SPPTs, and SNT synthesized using four different ratios of DI water to ODE. The drop-casting concentrations used for producing BPPTs, SPPTs and SNT were determined quantitatively and are reported in Tables S1 and S2. For BPPTs, the highest concentration (69 μg μl^{-1}) was obtained for the 1 : 0 ratio (DI water: ODE), while the lowest concentration (27.2 μg μl^{-1}) was observed for the 1 : 1 ratio, with the 1 : 0.5 and 1 : 0.25 ratios yielding comparable intermediate concentrations (61.8 μg μl^{-1} and 58.1 μg μl^{-1}). These concentration variations directly impact the resulting film morphology. Accordingly, BPPTs-derived films (Fig. S2a) exhibited rough and heterogeneous surfaces, with the dense dark-yellow domains observed for the 1 : 0 ratio (pure DI water) arising from the higher BPPTs loading and the presence of $CsPbBr_3$ as the dominant phase, whereas lower concentration samples (1 : 1, 1 : 0.5 and 1 : 0.25) displayed sparse deposition and visible white precipitates, which can be correlated with the increased detectability of the Cs_4PbBr_6 secondary phase in the corresponding XRD patterns (Fig. 3b).

In contrast, the SPPTs exhibited the highest concentration for the 1 : 1 ratio of DI water to ODE (70.9 μg μl^{-1}), followed by the 1 : 0.5 (38.1 μg μl^{-1}) and 1 : 0.25 ratios (30.9 μg μl^{-1}), while the 1 : 0 ratio showed the lowest concentration (16.3 μg μl^{-1}), as summarized in Tables S1 and S2. As a result, SPPTs-derived films (Fig. S2b) prepared with 1 : 1 ratio of DI water to ODE depicted the most uniform coverage, whereas the films prepared from the lower drop-casting concentrations displayed localized particle accumulation and discontinuous regions (Fig. S2b). A similar qualitative trend is observed for SNT-derived films (Fig. S2c), where the films prepared *via* 1 : 1 ratio of DI water to ODE showed visibly higher particle coverage,

 This journal is © The Royal Society of Chemistry 2026

Open Access Article. Published on 26 January 2026. Downloaded on 5/30/2026 3:48:49 AM. This article is licensed under a Creative Commons Attribution 3.0 Unported Licence.

while progressively reduced coverage is observed at lower ODE amounts. These observations for SNT are based on visual inspections rather than quantitative concentration measurements owing to the low particle yield in the supernatant fractions. Overall, these results demonstrate that synthesis-dependent variations in particle concentration play a dominant role in governing the resulting film's uniformity.

The films in this study were prepared by simple drop-casting and were not optimized for thickness or lateral uniformity, as evident from Fig. S2, and the resulting coatings are discontinuous and rough, reflecting both synthesis-dependent concentration variations (Tables S1 and S2) and the inherent limitations of drop-casting technique.[52] Consequently, the reported optical results represent ensemble-averaged emission from deposited particle (BPPTs, SPPTs and SNT) layers, rather than from device-grade continuous thin films. Further optimization of synthesis routes and deposition strategies will be required to achieve continuous films suitable for practical device applications.[53]

Fig. 4a–d shows PL characteristics of the prepared films (Fig. 4a and c), colloidal solutions (Fig. 4b), and supernatants (SNT) (Fig. 4d), which were prepared with different ratios of DI water to ODE. From Fig. 4a–d, the PL characteristics of the prepared films, colloidal solutions, and supernatants are analysed and presented in Fig. 4e–f for the PL peak intensity, peak wavelength, and FWHM (Full Width at Half Maximum), respectively.

For the films made from the BPPTs, increasing the ODE fraction causes the decrease of the PL peak intensity with the one prepared with pure DI water (1 : 0 ratio of DI water to ODE) delivering the most intense PL peak intensity, as shown in Fig. 4e. This can be attributed to the combined effects of the highest drop-casting concentration (69 μg μl^{-1}) in the 1 : 0 (pure DI water) BPPT sample and the formation of a predominantly single-phase orthorhombic $CsPbBr_3$ (Fig. 3a) with minimal surface-bound ligands. The absence of non-luminescent Cs_4PbBr_6 secondary phase also minimizes the effective non-radiative recombination pathways, resulting in enhanced radiative emission.[54]

For the films made from SPPTs, the PL peak intensity increases with increasing the ODE fraction, as shown in Fig. 4e. The film with the SPPTs prepared from the 1 : 1 ratio (DI water : ODE) delivers the highest PL peak intensity, which can be attributed to the combined effects of the highest drop-casting concentration (70.9 μg μl^{-1}) in this sample and the dominance of the $CsPbBr_3$ phase (Fig. 3b). Although a trace amount of the non-luminescent Cs_4PbBr_6 secondary phase is detected by XRD (Fig. 3b), its minimal presence does not significantly impact the overall radiative emission, allowing the PL intensity to remain maximized (Fig. 4e). A similar pattern has been observed for SNT-derived films (Fig. 4e), where the film prepared using a 1 : 1 ratio of DI water to ODE exhibited the highest PL peak intensity (Fig. 4e); however, their corresponding drop-casting concentrations were below the detection limit of the available instrumentation.

Fig. 4f and g summarize the dependence of the PL peak wavelength and FWHM on the DI water : ODE ratio used to synthesize BPPTs, SPPTs, and SNT particles. For BPPT-derived films, the PL maximum initially exhibited a pronounced blue-shift (from ~534 nm to ~526 nm) as the DI water : ODE ratio is varied from 1 : 0 to 1 : 0.5, shown in Fig. 4f, indicating a progressive suppression of aggregation-induced red-shift effects under biphasic growth conditions. A slight red-shift (to ~528 nm) observed for the 1 : 1 ratio of DI water to ODE (Fig. 4f) suggests the presence of competing solid-state optical processes, such as enhanced reabsorption or local particle accumulation under highly biphasic environments. However, the SPPT-derived films exhibited a relatively modest monotonic blue-shift (from ~528 nm to ~524 nm) as the DI water : ODE ratio is varied from 1 : 0 to 1 : 1 (Fig. 4f), consistent with their smaller particle size and weaker inter-particle optical coupling. Further, the SNT-derived films showed minor variations in PL peak positions (from ~521 nm to ~524 nm) with no clear monotonic trend as the DI water : ODE ratio was varied (Fig. 4f), which can be attributed to their low drop-casting concentration and limited solid-state interactions. Moreover, the linewidth values (Fig. 4g) displayed no pronounced systematic dependence on the ODE ratios, although BPPT0 exhibited the broadest emission, consistent with stronger aggregation-induced spectral broadening. In comparison, SPPTs and SNTs show relatively narrow and nearly invariant FWHM (variations <1–2 nm), indicating more homogeneous optical environments and reduced ensemble broadening effects.

Notably, the BPPT-derived films synthesized using pure water (1 : 0 ratio of DI water to ODE) exhibited a PL peak maximum at ~534 nm, which is red-shifted relative to PL emission wavelengths typically reported for well-dispersed $CsPbBr_3$ nanocrystals (~515–520 nm).[55,56] However, red-shifted PL emission (≥530 nm) has often been reported for solid-state $CsPbBr_3$ films.[57,58] For instance, Zalrhi, *et al.*[57] reported a PL emission peak at ~2.3 eV (~539 nm) for pristine $CsPbBr_3$ films deposited *via* spin coating at 5000 rpm for 30 s. Yeh, *et al.*[58] fabricated green-emitting $CsPbBr_3$ films *via* thermal evaporation, exhibiting PL emission at ~533 nm with narrow linewidth of <18 nm. Moreover, close packing in $CsPbBr_3$ films can induce a red-shit in PL emission wavelengths compared to less-coupled or dispersed counterparts, consistent with inter-particle optical coupling and radiative transfer in dense films.[59] Such red-shifts are further supported by photon-recycling behavior (self-absorption and re-emission), which has been explicitly shown to produce PL red shifts that increase with increasing emitter concentration and optical path length.[60] Therefore, the PL emission at ~534 nm observed for BPPT-derived films (1 : 0) can be attributed to the dense and heterogeneous drop-cast regions that enhance the reabsorption-re-emission processes and modify the ensemble emission profiles.

Based on their highest drop-casting concentration, strongest PL intensity (Fig. 4e), and dominant orthorhombic $CsPbBr_3$ phase (Fig. 3a), the 1 : 0 (pure DI water) BPPT and 1 : 1 (DI water: ODE) SPPT-derived films were selected as representative samples for all subsequent analyses and are hereafter referred to as "BPPT0" and "SPPT1", respectively. Notably, BPPT0 exhibits phase-pure orthorhombic $CsPbBr_3$ character (with no detectable amount of Cs_4PbBr_6 phase), whereas SPPT1 is

Open Access Article. Published on 26 January 2026. Downloaded on 5/30/2026 3:48:49 AM.
This article is licensed under a Creative Commons Attribution 3.0 Unported Licence.

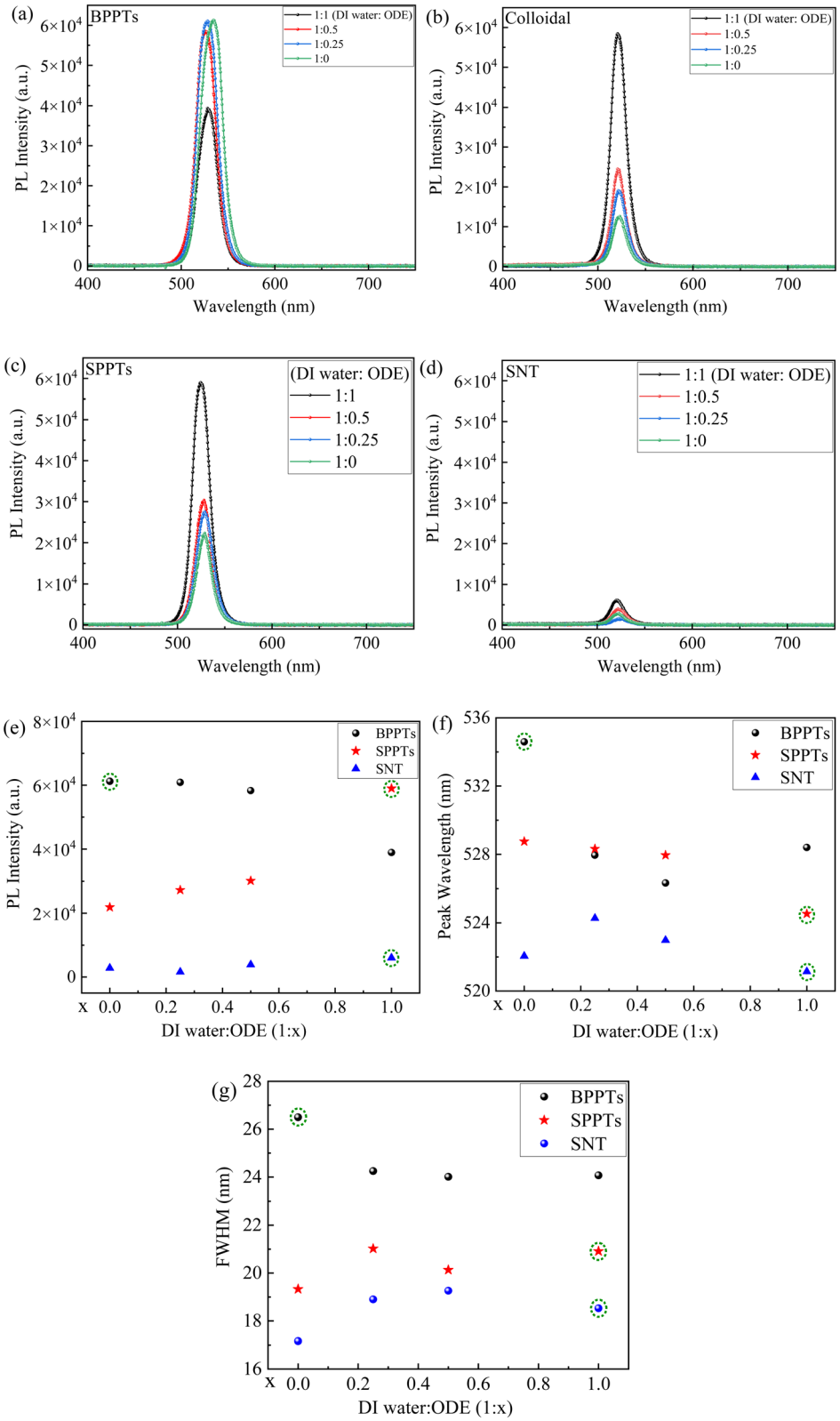

Fig. 4 PL spectra of (a) BPPTs, (b) colloidal solutions, (c) SPPTs, (d) SNT; variations of PL peak intensity (e), peak wavelength (f) and FWHM with the water : ODE ratio.

This journal is © The Royal Society of Chemistry 2026

Open Access Article. Published on 26 January 2026. Downloaded on 5/30/2026 3:48:49 AM.
This article is licensed under a Creative Commons Attribution 3.0 Unported Licence.

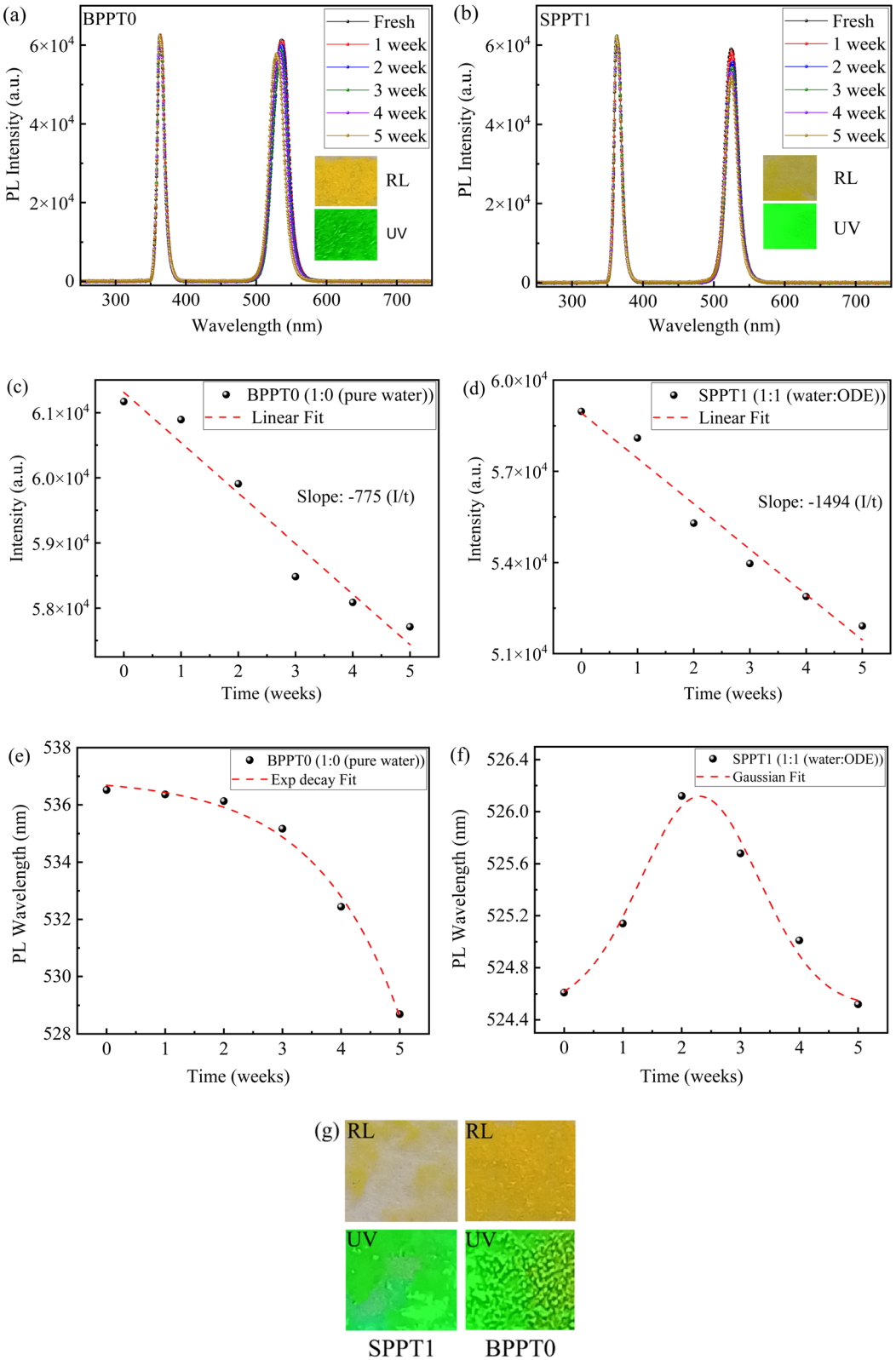

Fig. 5 PL spectra at different weeks for the films from (a) the BPTT0 prepared with pure water (inset: optical images of fresh films under room light (RL) and UV light (365 nm in wavelength)), (b) the SPPT1 prepared with the 1 : 1 ratio (inset: optical images of fresh films under RL and UV light); temporal evolution of PL intensity for the films from (c) the BPPT0 and (d) the SPPT1; temporal dependence of PL wavelength for the films from (e) the BPPT0 and (f) the SPPT1; and (g) optical images of the films from the SPPT1 prepared with the 1 : 1 ratio (left) and BPPT0 with pure water (right), after 5 weeks.

Open Access Article. Published on 26 January 2026. Downloaded on 5/30/2026 3:48:49 AM. This article is licensed under a Creative Commons Attribution 3.0 Unported Licence.

dominated by the orthorhombic $CsPbBr_3$ phase with only trace amounts of the secondary Cs_4PbBr_6 phase, as identified by their corresponding XRD spectra (Fig. 3a and b).

Fig. 5a and b shows the PL spectra over five weeks for the films from the BPTT0 prepared with pure water and the SPPT1 prepared with the 1 : 1 ratio, respectively. The insets in individual figures present optical images of corresponding fresh films under room light (RL) and UV light of 365 nm in wavelength. In general, the PL emission of the films remains relatively stable. Fig. 5c and d shows the temporal evolution of PL intensities for both the films, as derived from Fig. 5a and b The PL intensities of both the films exhibit a nearly linear decrease in PL intensity over the test period, indicating gradual photodegradation under ambient conditions (T ~18 °C, relative humidity (RH) ~60%, and normal indoor laboratory lighting). Under such exposure, metal-halide perovskites (including $CsPbBr_3$) are well known to undergo moisture-assisted degradation involving halide migration, surface defect formation, lattice distortion, and oxidation, which collectively enhance non-radiative recombination and suppress PL emission.[61–65]

Using the linear regression to fit the results in Fig. 5c and d, we obtain the degradation rates of 1494 and 775 in the unit of a.u. per week for the films from the SPPT1 and BPPT0, respectively. The films from the SPPT1 degrade nearly twice as fast as the ones from the BPPT0. Such faster degradation for smaller particles (SPPT1) is consistent with previous reports dictating the critical role of surface-to-volume ratio in determining the stability of perovskite materials.[66,67] Smaller particles can experience faster moisture and oxygen-induced degradation due to their higher surface defect densities and larger environmental exposure.

Importantly, $CsPbBr_3$ perovskites are highly susceptible to structural degradation when exposed to moisture, with water molecules disrupting the perovskite lattice and initiating decomposition pathways, ultimately degrading their optoelectronic properties.[68] For instance, Di Girolamo, *et al.*[69] reported a partial degradation of $CsPbBr_3$ perovskite phase under prolonged exposure to humidity, accompanied by the formation of secondary crystalline phases in these films, consistent with moisture-assisted phase evolution during aging.[68–72] These previously established degradation pathways[68–72] align well with the monotonic PL decay observed in Fig. 5c and d.

Interestingly, the PL peak wavelength for the film made from the BPPT0 exhibits different evolution from the one for the film made from the SPPT1, as shown in Fig. 5e and f. Precisely, the PL peak wavelength for the film made from the BPPT0 shows an exponential decay over time, indicating a continuous blue-shift of PL peak over time. The temporal evolution of the PL peak wavelength is fitted with a single exponential decay model, as shown in Fig. 5e. This blue-shift might arise due to a variety of mechanisms such as loss of surface halide, partial degradation of larger particles, or ion migration, defects formation and lattice distortions.[73–76] These factors are among unique properties of halide perovskites, which in this case result in the widening of band gap due to reduction in effective-negative antibonding overlap between 6 s Pb and 4p Br orbitals of $CsPbBr_3$ ultimately causing blue shift.[73–77] For instance, Phung, *et al.*[77] suggested that lattice distortions can cause the widening of band gap due to introduction of defects in $MaPbI_3$, leading to the blue shift of its PL peak.

In contrast, the PL peak wavelength for the film made from the SPPT1 depicts a non-monotonic PL peak shift, initially exhibiting red-shift followed by blue-shift over time. Such behavior resembles a Gaussian profile, which is well-fitted by a Gaussian function (Fig. 5f), and can be attributed to occurrence of multiple competing processes such as initial surface healing, trap-state passivation or possibly agglomeration. All these possibly cause the red shift. After the read shift, degradation-driven blue-shift might occur due to enhanced antibonding interactions between Pb and Br orbitals, leading to wider band gap and consequently.[73–77]

Overall, such results highlighted the relative photostability advantages of larger $CsPbBr_3$ particles (BPPT0) synthesized with pure water only, which offers slower degradation pathways and more predictable spectral evolution over time. In contrast, although, the films from the SPPT1 prepared with 1 : 1 ratio initially exhibit a higher PL intensity, they undergo rapid and more complex degradation dynamics due to their smaller size (high surface-to-volume ratio), higher defect density, and greater environmental reactivity.[66,67]

Fig. 5g shows optical images of BPPT0 and SPPT1-derived films after storage under ambient conditions (T ~18 °C and RH ~60%) for five weeks. The BPPT0-derived films retained relatively larger and more connected particle domains over time (Fig. S2a and 5g), consistent with the higher BPPT loading and larger particle sizes. In contrast, the SPPT1-derived films, which initially exhibits higher surface coverage (Fig. S2b), evolves into spatially separated particle domains distributed across the substrate after five weeks (Fig. 5g). This behaviour suggests progressive film fragmentation or island formation, which can be attributed to weaker interparticle cohesion, reduced effective film thickness, and the higher surface-area-to-volume ratio of the smaller SPPTs. These factors enhance the susceptibility to moisture- and oxygen-induced redistribution, leading to

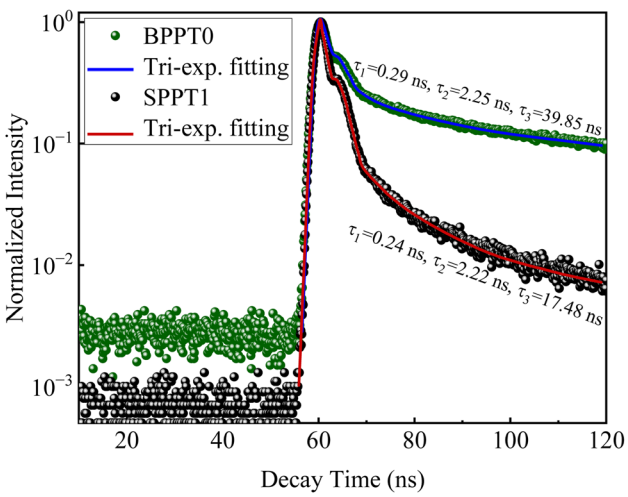

Fig. 6 Time-resolved PL decay curves for the films from the BPPT0 and SPPT1 synthesized with 1 : 0 (pure water) and 1 : 1 ratios, respectively.

 This journal is © The Royal Society of Chemistry 2026

Open Access Article. Published on 26 January 2026. Downloaded on 5/30/2026 3:48:49 AM.
This article is licensed under a Creative Commons Attribution 3.0 Unported Licence.

morphological instability over time. This interpretation is consistent with the comparatively faster PL degradation (Fig. 5d) and the associated Gaussian-like spectral evolution observed in Fig. 5f.

Fig. 6 shows the time-resolved PL decay curves for the films derived from the BPPT0 and SPPT1, and these curves can be fitted using tri-exponential decay model as given below:[78,79]

$$I_{TRPL} = A_1 e^{-t/\tau}{}_1 + A_2 e^{-t/\tau}{}_2 + A_3 e^{-t/\tau_3} \quad (1)$$

Here, A_i ($i = 1$, 2 and 3) and τ_i are the amplitude and lifetime of the i-th component, respectively.

For the BPPT0-derived film, three decay components were obtained using eqn (1) namely $\tau_1 = 0.29$ ns (6.75%), $\tau_2 = 2.26$ ns (15.97%), and $\tau_3 = 39.85$ ns (77.28%), yielding an amplitude-weighted average lifetime of $\langle\tau\rangle = 39.61$ ns with a reduced χ^2 of ~1.55. In contrast, the SPPT1-derived film exhibited $\tau_1 = 0.25$ ns (10.70%), $\tau_2 = 2.22$ ns (70.50%), and $\tau_3 = 17.48$ ns (18.80%), corresponding to $\langle\tau\rangle = 3.84$ ns with a reduced χ^2 of ~1.34 (Table S3). Based on both the lifetimes and their amplitude fractions, the longest decay component (τ_3) is assigned to band-edge radiative recombination, the intermediate component (τ_2) to surface-related recombination, and the fastest component (τ_1) to deep trap-assisted non-radiative recombination.[79,80] The

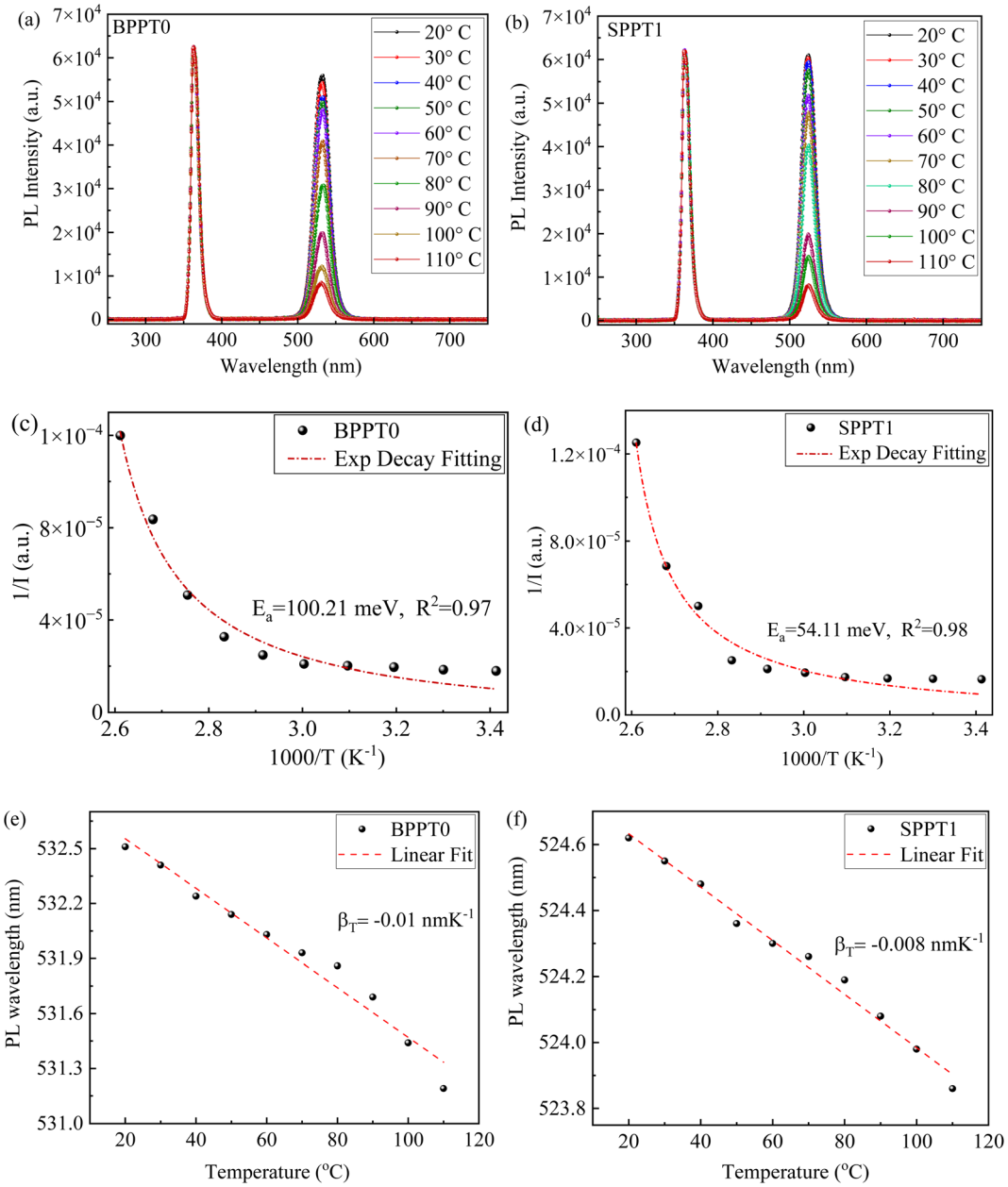

Fig. 7 PL spectra at different temperatures for the films prepared with the (a) BPPT0, and (b) SPPT1; variation of PL peak intensity with temperature for the films prepared with the (c) BPPT0, and (d) SPPT1; variation of PL wavelength with temperature for the films prepared with the (e) BPPT0, and (f) SPPT1.

Open Access Article. Published on 26 January 2026. Downloaded on 5/30/2026 3:48:49 AM.
This article is licensed under a Creative Commons Attribution 3.0 Unported Licence.

faster radiative rate for the SPPT1 ($\tau_3 = 17.48$ ns) compared to the larger BPPT0 ($\tau_3 = 39.85$ ns) is consistent with previous reports given by Abbas, *et al.*,[81] who concluded that radiative decay lifetime in weak confinement region decreases with decreasing particle size due to thermal accessibility to "dark" states for $CsPbBr_3$ materials with different phases including orthorhombic phase. Another factor for the higher radiative decay lifetime for the BPPT0 might be smaller surface area-to-volume ratio for the BPPT0 compared to the SPPT0 leading to lesser surface defect density and comparatively lesser non-radiative recombination routes.[82–84] The faster radiative lifetime for the film from the BPPT0 ($\tau_2 = 39.85$ ns), which were synthesized at room temperature (T ~16 °C), is significantly higher compared to other reports in literature for halide perovskite and other luminescent films. For instances, Bai, *et al.*[7] achieved a maximum radiative lifetime of ~6 ns *via* the annealing of $CsPbB_3$ films at a temperature of 460 °C. Tang, *et al.*[54] reported a radiative decay lifetime of ~17 ns for the $CsPbB_3$ thin films synthesized *via* antisolvent method with toluene being the antisolvent, which is noticeably lower than 39.85 ns for the film from the BPPT0 synthesized *via* pure water, noting the superiority of water as an antisolvent to produce $CsPbBr_3$ films of higher quality.

Fig. 7a and b depicts the PL curves at different temperature for the films from the BPPT0 and SPPT1 synthesised with 1 : 0 (pure water) and 1 : 1 ratios, respectively. Using the PL spectra, the variation of the corresponding PL peak intensity with temperature is presented in Fig. 7c and d, respectively, for the films. The decline in the PL peak intensity with rising temperature can be attributed to the increase of the dissociation of excitons and enhanced phonon scattering at higher temperatures, altering the carrier's effective masses leading to slower radiative recombination rates. Such phenomena of thermal quenching in PL intensity are common for most luminescent materials.[85–87] The temperature dependence of the PL peak intensity can be described by the following equation:[85–88]

$$I(T) = \frac{I(0)}{1 + Be^{-E_a/k_b T}} \quad (2)$$

where $I(T)$ and $I(0)$ are the PL peak intensities at temperatures of T and 0 K, respectively, B is a constant, k_b is the Boltzmann constant, and E_a is the activation energy.

The temperature dependence of the PL intensity for the films (Fig. 7c and d) are curve-fitted with eqn (2), yielding thermal activation energies of 100.21 meV and 54.11 meV for the films made from the BPPT0 and SPPT1, respectively. These fitted activation

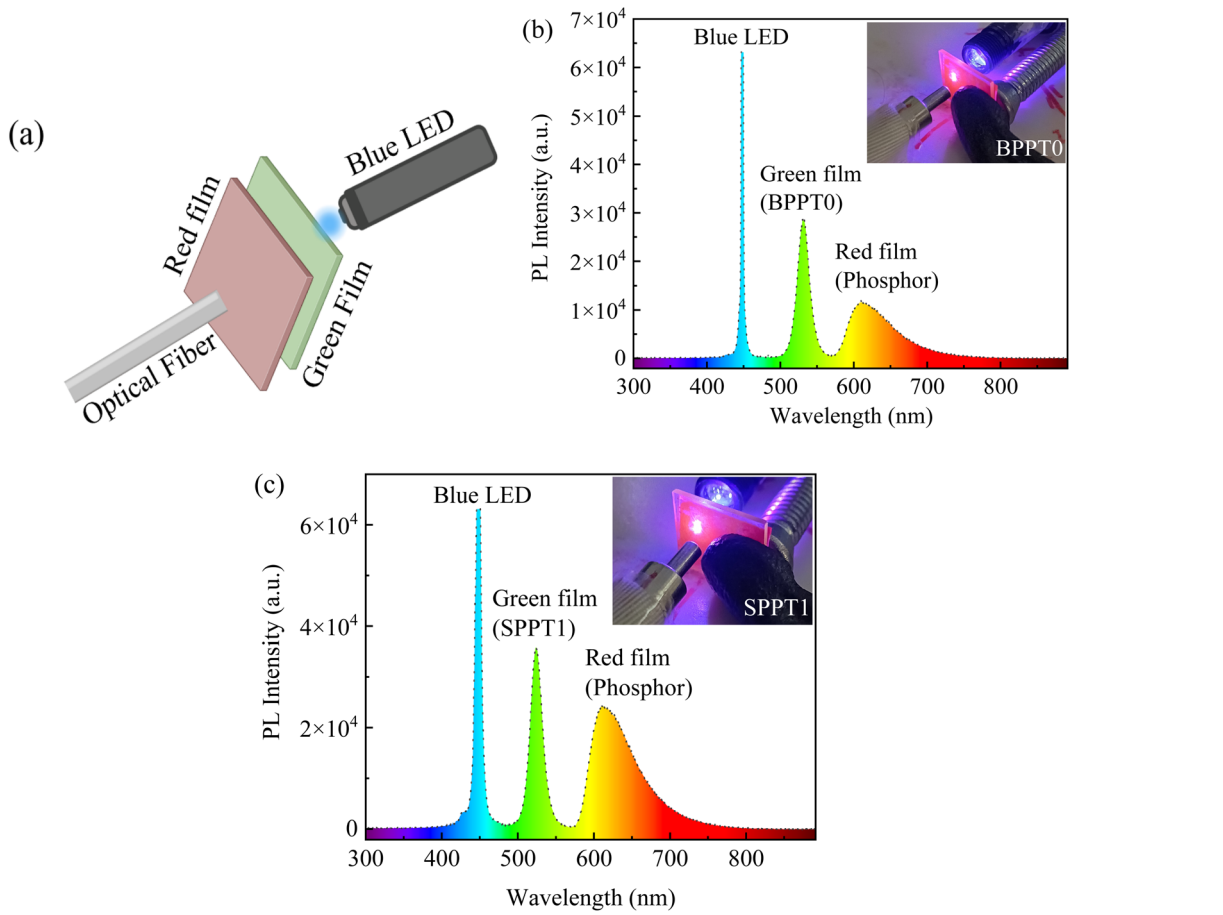

Fig. 8 (a) Schematic illustration of the experimental setup for the RGB backlight configuration (R: red phosphor film, G: green emitting perovskite film (SPPT1/BPPT0), B: blue LED); PL spectra for white emitting backlight using (b) BPPT0 and (c) SPPT1 green films (insets: optical images of white emitting backlight structures).

 This journal is © The Royal Society of Chemistry 2026

Open Access Article. Published on 26 January 2026. Downloaded on 5/30/2026 3:48:49 AM.
This article is licensed under a Creative Commons Attribution 3.0 Unported Licence.

energies can be interpreted as the effective thermal barriers for PL quenching (energy required to activate competing non-radiative recombination pathways), rather than the intrinsic exciton binding energy of $CsPbBr_3$ perovskite structures.[89–93] For bulk and high-quality $CsPbBr_3$ perovskites, the intrinsic exciton binding energies are typically reported in the range of ~18–44 meV, as determined from optical and magneto-optical spectroscopy studies of perovskite single crystals and thin films.[91–93] In contrast, the larger values obtained for BPPT0 (~100.21 meV) and SPPT1 (~54.11 meV) may reflect the combined influence of thermally activated carrier trapping, exciton delocalization, and phonon-assisted non-radiative recombination processes in these micron-sized $CsPbBr_3$ based particles.[89] Further, the higher activation energy observed in BPPT0 (~100.21 meV) indicates that non-radiative pathways are less readily thermally activated in the larger particles in contrast to SPPT1 where a lower value of activation energy (~54.11 meV) can be attributed to the higher surface-to-volume ratio of the smaller particles, increasing the density of surface-associated trap states and facilitating thermally induced PL quenching at lower energies.[94] This is consistent with longer radiative lifetime observed in BPPT0 ($\tau_3 = 39.85$ ns) compared to SPPT1 ($\tau_3 = 17.48$ ns) (Fig. 6), indicating suppressed non-radiative recombination pathways in the larger BPPT0 particles.

Fig. 7e and f shows the linear temperature dependence of the PL peak wavelength for the films from the BPPT0 and SPPT1 synthesised with 1 : 0 (pure water) and 1 : 1 ratios, respectively, which depicts blue-shift with increasing temperature and can be described by the following equation:[85]

$$\lambda(T) = \lambda(T_0) + \beta_T \Delta T \quad (3)$$

for $|\Delta T/T_0| \ll 1$. Here, $\lambda(T)$ and $\lambda(T_0)$ are the PL peak wavelengths at temperature T and a reference temperature T_0, and β_T is a factor determining the temperature dependence of the PL peak wavelength. Using eqn (3) to fit the data in Fig. 7e and f, we obtain the numerical values of β_T as -0.01 nmK^{-1} and -0.008 nmK^{-1} for the films from the BPPT0 and SPPT1 synthesised with 1 : 0 (pure water) and 1 : 1 ratios, respectively.

The blue shift of the PL wavelength can be attributed to various factors, such as enhanced electron–phonon interactions at higher temperatures, thermally induced defects, lattice distortions *etc.*, which hinder the negative antibonding overlapping of 6s Pb and 4p Br orbitals of orthorhombic $CsPbBr_3$ and increases the band gap.[73–77,95] A smaller numerical value of β_T for the film from the BPPT0 compared to the one from the SPPT1 points towards better PL stability of the BPPT0 compared to the SPPT1 likely due to reduced electron–phonon interactions,[95] which is consistent with a longer radiative decay lifetime ($\tau_3 = 39.85$ ns) and a lower rate of degradation (−775) for the BPPT0 synthesized *via* pure water.

Fig. 8 presents a qualitative proof-of-concept demonstration of white light generation by combining the green emission from $CsPbBr_3$-based particles (BPPT0 and SPPT1) with complementary red and blue fluorescent components. A commercial red EXPO fluorescent marker was employed as a readily available broadband red emitter to verify spectral overlap and color-mixing capability rather than to serve as a device-optimized red phosphor. Using the films made from the BPPT0 (λ ~532 nm) and SPPT1 (λ ~524 nm) with a red emissive phosphor film (λ ~610 nm) and following the approach reported by Tang, *et al.*,[85] we constructed a qualitative 'white' emitting LCD backlight configuration (Fig. 8a). The LCD backlight structure was activated by a blue LED (~450 nm in wavelength). Fig. 8b and c shows the corresponding PL emission spectra of the resulting 'white' backlights based on BPPT0 and SPPT1. The insets depict optical images of the corresponding backlight structures emitting bright white light, similar to the one demonstrated by Tang, *et al.*,[85] who mimicked a white-emitting LCD backlight structure using a green-emitting PMMA-$PbBr_3$ film with PL emission peak at ~537 nm.

4 Discussions

The layered water/ODE system offers a biphasic environment with a water-ODE interface, in which ODE forms a non-polar

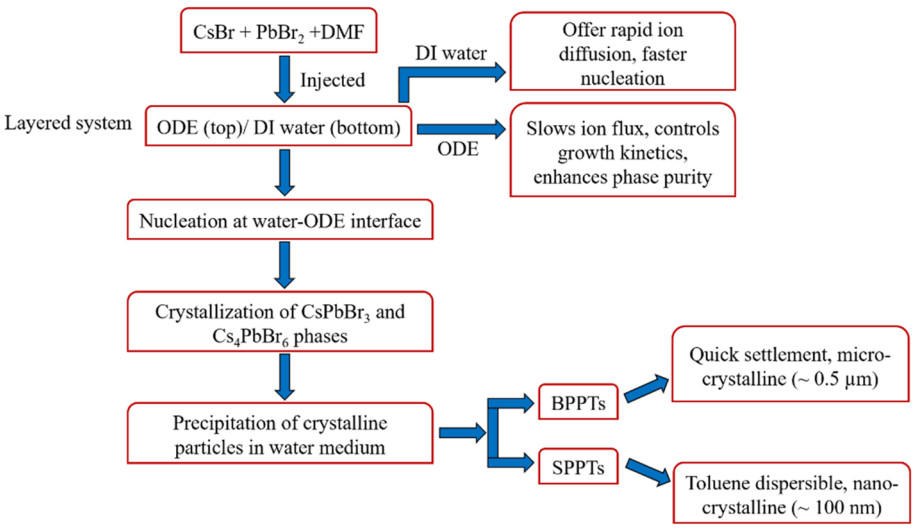

Fig. 9 A flowchart for the formation and growth of $CsPbBr_3$ particles in a water/ODE layered system.

Open Access Article. Published on 26 January 2026. Downloaded on 5/30/2026 3:48:49 AM. This article is licensed under a Creative Commons Attribution 3.0 Unported Licence.

layer over polar water layer. Such a system likely separates the nucleation and growth of orthorhombic $CsPbBr_3$ particles spatially. Upon injecting the DMF precursor with CsBr, $PbBr_2$ and small amounts of ligands, nucleation occurs at the ODE-water interface, as supported by the presence of green emitting particles. Polar water quickly solvates precursor ions, promoting nucleation and growth of $CsPbBr_3$ particles, while non-polar ODE layer modulates the diffusion of ions across the interface. The amount of ODE plays a pivotal role in dictating ionic diffusion, nucleation zone, crystal growth, and consequently, the particle size, phase as well as PL behaviour of final obtained particles. A flowchart summarizing the chemical kinetics involved in this water/ODE layered system is presented in Fig. 9, respectively.

For the BPPTs, formed predominantly *via* rapid growth kinetics, the chemical reaction generally follows the stoichiometric perovskite formation as:

$$CsBr + PbBr_2 \rightarrow CsPbBr_3 \quad (4)$$

In a pure water system, the absence of ODE leads to fast and homogeneous mixing of precursor ions in this aqueous medium, resulting in uncontrolled nucleation and formation of large bulk precipitates (BPPT0) which were settled at the bottom and exhibited pure orthorhombic $CsPbBr_3$ phase with no detectable trace of Cs_4PbBr_6 phase, as verified by XRD (Fig. 3a). However, increasing the ODE amount (ratios of 1 : 0.25, 1 : 0.5, and 1 : 1 for water: ODE systems) led to excess CsBr availability from altered solvation and ion diffusion dynamics which led to partial formation of the Cs-rich Cs_4PbBr_6 phase with reaction involved below:

$$CsPbBr_3 + 3CsBr \rightleftarrows Cs_4PbBr_6 \quad (5)$$

The coexistence of double phases is not only evidenced by the XRD peaks depicted in Fig. 3a but also is well reported in literature.[47–49]

For SPPTs, which consist of smaller particles with higher surface-area-to-volume ratios, the detectability of secondary phases (such as Cs_4PbBr_6) was observed to be more sensitive to local chemical fluctuations and drop-casting concentrations. In the pure DI water system, the limited solubility of $PbBr_2$ and reduced ionic transport across the reaction environment may promote local compositional inhomogeneity, leading to the emergence of detectable Cs_4PbBr_6 secondary reflections alongside the dominant orthorhombic $CsPbBr_3$ phase. Introduction of ODE creates a biphasic environment that moderates nucleation and growth dynamics at the water-ODE interface, thereby influencing the effective particle concentration of the resulting dispersions. Accordingly, the SPPT1 sample prepared with 1 : 1 ratio of DI water to ODE, which also exhibits the highest drop-casting concentration (Tables S1 and S2) among other SPPTs, shows the strongest green PL emission (Fig. 4e), while $CsPbBr_3$ remains the dominant phase with only trace amounts of Cs_4PbBr_6 secondary phase.

All subsequent studies have been focused on the films from the BPPT0 prepared with pure water and the SPPT1 prepared with the 1 : 1 ratio according to the combinational factors of particle size, phase purity, and optical performance. In the pure water system (BPPT0), the absence of ODE allows for rapid nucleation and uncontrolled growth of crystals due to the lack of interfacial stabilization. This results in the formation of larger $CsPbBr_3$ precipitates of ~500 nm (Fig. 2a) with no detectable amounts of non-luminescent Cs_4PbBr_6 phases (Fig. 3a). In contrast, the biphasic system of the 1 : 1 ratio (SPPT1) offers a more balanced environment for the formation and growth of $CsPbBr_3$ due to presence of the water-ODE interface, which effectively moderates the nucleation and growth process. This results in formation of smaller $CsPbBr_3$ precipitates of ~100 nm (Fig. 2b) with enhanced colloidal stability and stronger green emission, alongside formation of hexagonal Cs_4PbBr_6, as confirmed by the XRD analysis (Fig. 3b).

Fig. S3 in SI shows the absorbance and PL spectra for the films made from the BPPT0 and SPPT1 films. It is evident that there exists size dependence of the absorption and PL emission under UV light of ~365 nm in wavelength. The SPPT1 exhibit an absorption peak at ~521 nm and a PL emission peak at ~524 nm, leading to a Stokes shift of ~20 meV; the BPPT0 depict an absorption peak at ~524 nm and a PL emission peak at ~534 nm, leading to a Stokes shift of ~50 meV. This further suggests the inverse dependence of Stokes shift on particle size, which are well reported in multiple experimental and theoretical studies for many perovskite materials including $CsPbB_3$ particles.[96–98]

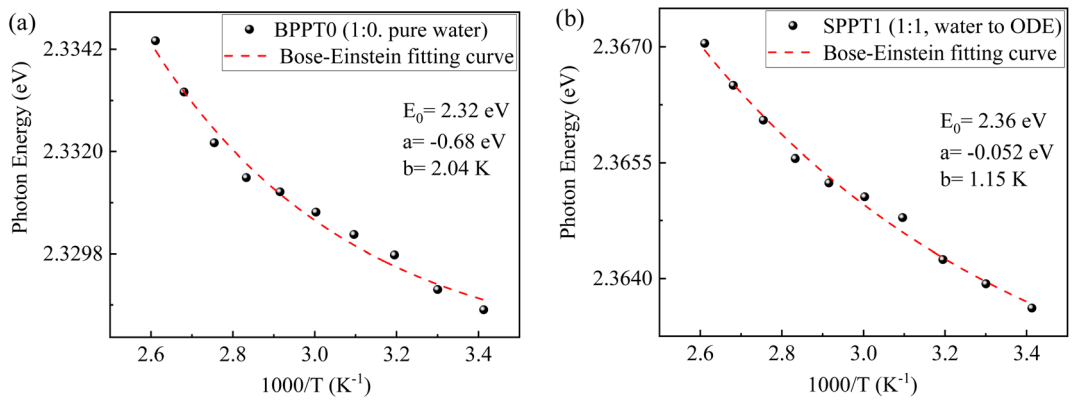

Fig. 10 Temperature dependence of photon energy for the (a) BPPT0 and (b) SPPT1.

 This journal is © The Royal Society of Chemistry 2026

Open Access Article. Published on 26 January 2026. Downloaded on 5/30/2026 3:48:49 AM.
This article is licensed under a Creative Commons Attribution 3.0 Unported Licence.

The difference between the band gap (E_g) of 2.36 eV for the SPPT1 and 2.31 eV for the BPPT0 at ~16 °C reveals the size dependence of optical properties of orthorhombic $CsPbBr_3$. Such a small difference in band gap with the size difference of ~400 nm between the SPPT1 and the BPPT0 might be attributed to the weaker confinement effect due to large difference between the particle sizes (both the SPPT1 and BPPT0) and the Bohr radius of $CsPbBr_3$.[99,100] Thereafter, the temperature dependence of band gap for both the BPPT0 (Fig. 10a) and the SPPT1 (Fig. 10b) are fitted with the Bose–Einstein relation as:[101–103]

$$E(T) = E_0(T) - \frac{2a}{e^{b/T} - 1} \quad (6)$$

where E_0 (T) represents the band gap at absolute zero, a describes the strength of electron–phonon interaction, and b is the characteristic temperature linked to average photon energy.

Eqn (6) is used to fit the temperature dependence of the band gap, as shown in Fig. 10a and b. It is evident that the parameter 'a' is negative for both the BPPT0 and SPPT1, revealing different behaviour of these $CsPbBr_3$ particles from the trend revealed by Huang, *et al.*,[103] who recently reported an decreasing trend of the band gap with increasing temperature (positive 'a') for $CsPbBr_3$ films with grain size of ~0.52 μm and reduced electron–phonon interaction (lower 'a') for larger particles. However, the increasing trend of the band gap with increasing temperature is similar to PbS and PbSe quantum dots,[95] and such behaviour has also been observed for all inorganic perovskite materials. For instance, Li, *et al.*[95] reported the increase in the band gap of $CsPbBr_3$ particles (E_g = 2.35 eV to 2.39 eV) with increasing temperature from 80 K to 300 K) with the increase rate of the band gap depends inversely on the particle size.

The temperature dependence of FWHM (Fig. 11a and b) is analysed for both the films using the Bose model as:[104,105]

$$\mathrm{FWHM}(T) = \Gamma_0 + \alpha T + \frac{\beta}{e^{\hbar w/kT} - 1} \quad (7)$$

where Γ_0 represents inhomogeneous broadening at 0 K, α refers to the degree of phonon scattering, β denotes the coupling strength between excitons and longitudinal optical (LO) phonons, and $\hbar\omega$ corresponds to LO phonon energy respectively. The fitting results with eqn (7) are also included in Fig. 11a and b, respectively.

According to the fitting results given in Fig. 11a and b, the LO phonon coupling energy of the BPPT0 is ~43 meV higher than ~25 meV of the SPPT1) and further higher the one given by Huang, *et al.*,[103] who reported an LO phonon coupling energy of ~20 meV for PMMA-$CsPbBr_3$ films with $CsPbBr_3$ of micron sizes (~0.5 μm) synthesized *via* a mechanochemical method. Such a higher value of the coupling energy might attribute to the combination of internal stresses, reduced structural disorder, and modified chemical environments introduced *via* the polar-nonpolar water: ODE systems. This result suggests the sensitivity of the LO phonon dynamics altered with subtle variations in the nucleation and growth pathways and highlights the importance of the synthesis conditions in tailoring optoelectronic behaviour of emissive particles.

According to Fig. 8b and c, the white emitting LCD backlight structures depict different results owing to the use of different particle sizes in the green-emissive films. For instance, the backlight structures constructed from the films with the BPPT0 exhibited 'colder' white emission, as evident by the higher colour coordinated temperature (CCT) of ~5317 K, in comparison to 'warmer' white light emitted by the backlight structures constructed from the films with the SPPT1 (CCT ~4317 K). Generally, a warmer white light (lower CTT) is usually preferred due to lesser amount of biological damages caused when perceived by human eyes such as reduced cell viability, cell cycle arrest, severe DNA damage *etc.*[106] All these give an edge to the SPPT1 over the BPPT0.

The colour gamut coverage areas of white light emitted by the backlight structures were calculated using Commission Internationale de l'Eclairage (CIE) colour coordinates. The backlight light structure constructed from the films with the SPPT1 spans relatively a higher colour gamut area of ~123% of NTSC 1953 and ~174% of sRGB (Fig. 12b), in comparison to a colour gamut coverage of ~112% of NTSC 1953 and ~158% of sRGB (Fig. 12a) for the backlight light structure constructed from the films with the BPPT0. Such a result not only highlights the dependence of gamut coverage area with the particle size of films employed to construct LCD backlight structures but also

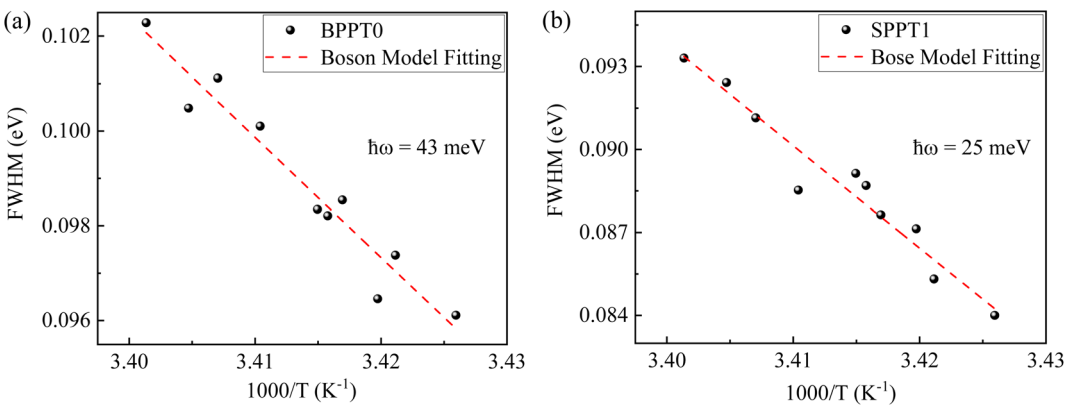

Fig. 11 Temperature dependence of FWHM with the fitting of Bose model (red dotted curve) for the films made from (a) BPPT0 and (b) SPPT1.

Open Access Article. Published on 26 January 2026. Downloaded on 5/30/2026 3:48:49 AM.
This article is licensed under a Creative Commons Attribution 3.0 Unported Licence.

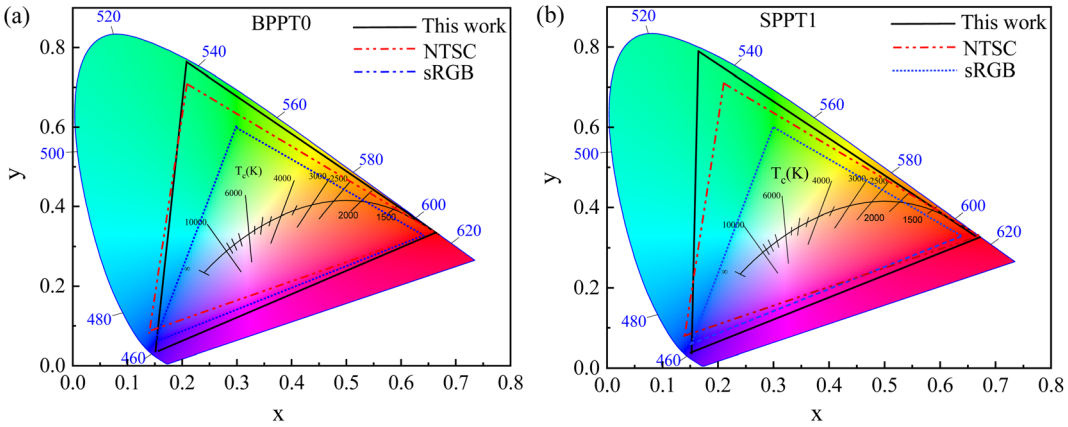

Fig. 12 CIE colour gamut coverage of the white emitting backlight structures constructed from the films with (a) BPPT0 and (b) SPPT1.

marks the potential of the SPPT1 and BPPT0 synthesized *via* the water: ODE system for applications in LCD display.

Table 1 compares the optical properties of BPPT0 and SPPT1-derived films with representative literature reports on $CsPbBr_3$ quantum dots, nanocrystals, composite systems, and thin films fabricated using spin-coating, vacuum deposition, thermal evaporation, and single-source vapor deposition methods. Notably, the present aqueous interface-directed synthesis yields films exhibiting narrow PL peaks at ~534 nm (BPPT0) and ~524 nm (SPPT1), with longer radiative decay lifetimes of up to ~100.21 ns (BPPT0) and ~54.11 ns (SPPT1) and significant thermal activation energies (~100.21 meV for BPPT0 and ~54.11 meV for SPPT1), which are comparable to those reported for conventionally processed $CsPbBr_3$ films. Furthermore, a comparison among different green emitting films,[107–117] utilized in fabrication of white LCD backlight structures, is

Table 1 Comparison of optical properties of $CsPbBr_3$-based emitters reported in literature and in this work

Study	Material/Processing	PL peak (nm)	FWHM (nm)	Radiative decay lifetime (τ_3) (ns)	Thermal activation energy (E_a) (meV)	Applications
Qaid, *et al.*[118]	$CsPbBr_3$ quantum dots (QDs) and thin films/spin coating	515	15	14.9	—	Lasers with low energy density threshold of amplified spontaneous emission (22.25 μJ cm^{-2})
Zalrhi, *et al.*[57]	$CsPbBr_3$ films/spin coating	~539	20.66	—	60.50	—
He, *et al.*[119]	$CsPbBr_3$ nanocrystals (NCs) and $CsPbBr_3$-Cs_4PbBr_6 composite NCs/one-pot method	519 and 515	36 and 33	—	—	LEDs with luminous efficiency of 45 lmW^{-1} at a 10 mA driving current
Bai, *et al.*[7]	$CsPbBr_3$ films/thermal co-evaporation	517	18	0.79 (average)	—	LEDs with maximum luminance of ~252 cdm^{-2}
Yeh, *et al.*[58]	$CsPbBr_3$ films/single-source vapor deposition process	533	<18	—	—	LEDs with maximum luminance of ~14 079 cd m^{-2}
Xiang, *et al.*[46]	$CsPbBr_3$ films/vacuum deposition	525	17	—	25.97 ± 2.99	LEDs with maximum luminance of 51 933 cd m^{-2} and wide gamut coverage area of ~114% of NTSC standard
Huang, *et al.*[103]	PMMA-$CsPbBr_3$ films/ mechanochemical-ultrasonic method	538	~29	46.99	217.48	—
Our work	BPPT0-derived film	534	26.5	39.85	100.21	LCD backlight structures with wide gamut coverage of ~112% of NTSC 1953 standards
Our work	SPPT1-derived film	524	20.9	17.48	54.11	LCD backlight structures with wide gamut coverage of ~123% of NTSC 1953 standards

 This journal is © The Royal Society of Chemistry 2026

Open Access Article. Published on 26 January 2026. Downloaded on 5/30/2026 3:48:49 AM.
This article is licensed under a Creative Commons Attribution 3.0 Unported Licence.

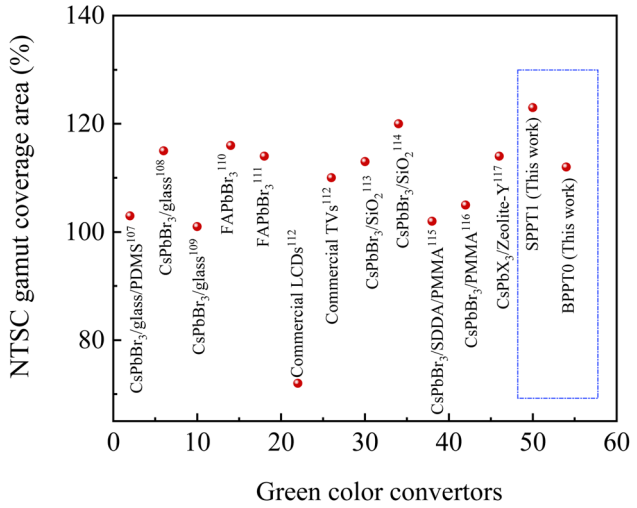

Fig. 13 Relative NTSC gamut coverage areas of LCD backlight structures with different green emitting films.

made in terms of the CIE colour gamut coverage area with respect to NTSC standard and is shown correspondingly in Fig. 13. It is clearly evident that the films prepared with SPPT1 in this work outperform other reported works while the films prepared with BPPT0 remain competitive relatively, making them excellent candidates for next generation display applications.

5 Conclusions

In summary, we have synthesized multi-sized $CsPbBr_3$-based particles using the biphasic water: ODE system. The ODE serves not just as a non-polar passive solvent, but also as a kinetic barrier that enables interface-confined nucleation and formation of smaller, relatively phase-purer, and more luminescent $CsPbBr_3$-based particles. Such a system allows tunability across phase composition ($CsPbBr_3$ *vs.* Cs_4PbBr_6), particle size (BPPTs *vs.* SPPTs), and opto-electronic behavior (PL, thermal stability, decay behavior, CCT and gamut coverage area of LCD backlights *etc.*), by simply varying the amount of ODE in the water: ODE system. It offers a versatile mechanism for designing next-generation perovskite materials with controlled opto-electronic behavior.

Conflicts of interest

The authors declare no competing financial interest.

Data availability

All possible experimental and analysed results have been included in this manuscript explicitly. No other new data has been generated by any further experiments/analyzation.

Supplementary information (SI) is available. See DOI: https://doi.org/10.1039/d5ta07491f.

Acknowledgements

FY is grateful for the support by the NSF through the CBET-2018411 monitored by Dr Nora F Savage.

References

1 B. Conings, J. Drijkoningen, N. Gauquelin, A. Babayigit, J. D'Haen, L. D'Olieslaeger, A. Ethirajan, J. Verbeeck, J. Manca and E. Mosconi, Intrinsic thermal instability of methylammonium lead trihalide perovskite, *Adv. Energy Mater.*, 2015, **5**(15), 1500477.
2 Y. Dong, T. Qiao, D. Kim, D. Parobek, D. Rossi and D. H. Son, Precise control of quantum confinement in cesium lead halide perovskite quantum dots via thermodynamic equilibrium, *Nano Lett.*, 2018, **18**(6), 3716–3722.
3 N. Wang, L. Cheng, R. Ge, S. Zhang, Y. Miao, W. Zou, C. Yi, Y. Sun, Y. Cao and R. Yang, Perovskite light-emitting diodes based on solution-processed self-organized multiple quantum wells, *Nat. Photonics*, 2016, **10**(11), 699–704.
4 A. Tiwari, N. S. Satpute, C. M. Mehare and S. Dhoble, Challenges, recent advances and improvements for enhancing the efficiencies of ABX3-based PeLEDs (perovskites light emitting diodes): A review, *J. Alloys Compd.*, 2021, **850**, 156827.
5 W. Chen, J. Zhang, G. Xu, R. Xue, Y. Li, Y. Zhou, J. Hou and Y. Li, A semitransparent inorganic perovskite film for overcoming ultraviolet light instability of organic solar cells and achieving 14.03% efficiency, *Adv. Mater.*, 2018, **30**(21), 1800855.
6 J. Zhang, G. Hodes, Z. Jin and S. Liu, All-inorganic CsPbX3 perovskite solar cells: progress and prospects, *Angew. Chem., Int. Ed.*, 2019, **58**(44), 15596–15618.
7 T. Bai, S. Wang, L. Bai, K. Zhang, C. Chu and L. Yi, Vacuum evaporation of high-quality CsPbBr3 thin films for efficient light-emitting diodes, *Nanoscale Res. Lett.*, 2022, **17**(1), 69.
8 K. P. Goetz and Y. Vaynzof, The challenge of making the same device twice in perovskite photovoltaics, *ACS Energy Lett.*, 2022, **7**(5), 1750–1757.
9 P. Fassl, V. Lami, A. Bausch, Z. Wang, M. T. Klug, H. J. Snaith and Y. Vaynzof, Fractional deviations in precursor stoichiometry dictate the properties, performance and stability of perovskite photovoltaic devices, *Energy Environ. Sci.*, 2018, **11**(12), 3380–3391.
10 G. W. Kim and A. Petrozza, Defect tolerance and intolerance in metal-halide perovskites, *Adv. Energy Mater.*, 2020, **10**(37), 2001959.
11 M. Kim, G.-H. Kim, T. K. Lee, I. W. Choi, H. W. Choi, Y. Jo, Y. J. Yoon, J. W. Kim, J. Lee and D. Huh, Methylammonium chloride induces intermediate phase stabilization for efficient perovskite solar cells, *Joule*, 2019, **3**(9), 2179–2192.
12 A. F. Castro-Méndez, J. Hidalgo and J. P. Correa-Baena, The role of grain boundaries in perovskite solar cells, *Adv. Energy Mater.*, 2019, **9**(38), 1901489.
13 J. He, H. Li, C. Liu, X. Wang, Q. Zhang, J. Liu, M. Wang and Y. Liu, Hot-Injection Synthesis of Cesium Lead Halide

Open Access Article. Published on 26 January 2026. Downloaded on 5/30/2026 3:48:49 AM. This article is licensed under a Creative Commons Attribution 3.0 Unported Licence.

Perovskite Nanowires with Tunable Optical Properties, *Materials*, 2024, **17**(10), 2173.

14 A. G. Muradova, U. A. Stepanova, T. V. Koroleva, K. T. Khakimov, K. I. Runina, K. A. Cherednichenko and A. V. Finko, Preparation of CsPbBr3/Cs4PbBr6 perovskite particles by modified hot injection method, *Nano-Struct. Nano-Objects*, 2025, **42**, 101487.

15 E. Ruby, H. Levy-Falk, G. Trippé-Allard, F. Fossard, M. Vallet, N. Guiblin, J.-S. Lauret, E. Deleporte and C. R. Mayer, Influence of arylalkyl amines on the formation of hybrid CsPbBr 3 nanocrystals via a modified LARP method, *Nanoscale Adv.*, 2024, **6**(6), 1704–1719.

16 C. K. Ng, C. Wang and J. J. Jasieniak, Synthetic evolution of colloidal metal halide perovskite nanocrystals, *Langmuir*, 2019, **35**(36), 11609–11628.

17 G. B. Nair, S. Tamboli, R. Kroon, S. Dhoble and H. C. Swart, Facile room-temperature colloidal synthesis of CsPbBr3 perovskite nanocrystals by the emulsion-based ligand-assisted reprecipitation approach: tuning the color-emission by the demulsification process, *J. Alloys Compd.*, 2022, **928**, 167249.

18 C. K. Ng, W. Yin, H. Li and J. J. Jasieniak, Scalable synthesis of colloidal CsPbBr 3 perovskite nanocrystals with high reaction yields through solvent and ligand engineering, *Nanoscale*, 2020, **12**(8), 4859–4867.

19 A. Soultati, M. Tountas, K. K. Armadorou, A. R. bin Mohd Yusoff, M. Vasilopoulou and M. K. Nazeeruddin, Synthetic approaches for perovskite thin films and single-crystals, *Adv. Energy Convers.*, 2023, **2**(8), 1075–1115.

20 X. Li, F. Cao, D. Yu, J. Chen, Z. Sun, Y. Shen, Y. Zhu, L. Wang, Y. Wei and Y. Wu, All inorganic halide perovskites nanosystem: synthesis, structural features, optical properties and optoelectronic applications, *Small*, 2017, **13**(9), 1603996.

21 M. V. Kovalenko, L. Protesescu and M. I. Bodnarchuk, Properties and potential optoelectronic applications of lead halide perovskite nanocrystals, *Science*, 2017, **358**(6364), 745–750.

22 H. Huang, M. I. Bodnarchuk, S. V. Kershaw, M. V. Kovalenko and A. L. Rogach, Lead halide perovskite nanocrystals in the research spotlight: stability and defect tolerance, *ACS Energy Lett.*, 2017, **2**(9), 2071–2083.

23 Y. Iso and T. Isobe, Synthesis, luminescent properties, and stabilities of cesium lead halide perovskite nanocrystals, *ECS J. Solid State Sci. Technol.*, 2017, **7**(1), R3040.

24 A. Kipkorir, J. DuBose, J. Cho and P. V. Kamat, CsPbBr 3–CdS heterostructure: Stabilizing perovskite nanocrystals for photocatalysis, *Chem. Sci.*, 2021, **12**(44), 14815–14825.

25 B. Akbali, G. Topçu, T. Guner, M. Ozcan, M. M. Demir and H. Sahin, CsPbBr 3 perovskites: Theoretical and experimental investigation on water-assisted transition from nanowire formation to degradation, *Phys. Rev. Mater.*, 2018, **2**(3), 034601.

26 L. Ndlwana, N. Raleie, K. M. Dimpe, H. F. Ogutu, E. O. Oseghe, M. M. Motsa, T. A. Msagati and B. B. Mamba, Sustainable hydrothermal and solvothermal synthesis of advanced carbon materials in multidimensional applications: a review, *Materials*, 2021, **14**(17), 5094.

27 K. Martina, G. Cravotto and R. S. Varma, Impact of microwaves on organic synthesis and strategies toward flow processes and scaling up, *J. Org. Chem.*, 2021, **86**(20), 13857–13872.

28 S. Li, H. Ma, P. Ouyang, Y. Li, Y. Duan, Y. Zhou, W.-J. Ong and F. Dong, Advanced microwave synthesis strategies for innovative photocatalyst design, *Green Energy Environ.*, 2025, **10**(8), 1597–1623.

29 T. Leijtens, K. Bush, R. Cheacharoen, R. Beal, A. Bowring and M. D. McGehee, Towards enabling stable lead halide perovskite solar cells; interplay between structural, environmental, and thermal stability, *J. Mater. Chem. A*, 2017, **5**(23), 11483–11500.

30 X. Gong, M. Li, X. B. Shi, H. Ma, Z. K. Wang and L. S. Liao, Controllable perovskite crystallization by water additive for high-performance solar cells, *Adv. Funct. Mater.*, 2015, **25**(42), 6671–6678.

31 S. Pathak, A. Sepe, A. Sadhanala, F. Deschler, A. Haghighirad, N. Sakai, K. C. Goedel, S. D. Stranks, N. Noel and M. Price, Atmospheric influence upon crystallization and electronic disorder and its impact on the photophysical properties of organic–inorganic perovskite solar cells, *ACS Nano*, 2015, **9**(3), 2311–2320.

32 G. E. Eperon, S. N. Habisreutinger, T. Leijtens, B. J. Bruijnaers, J. J. van Franeker, D. W. DeQuilettes, S. Pathak, R. J. Sutton, G. Grancini and D. S. Ginger, The importance of moisture in hybrid lead halide perovskite thin film fabrication, *ACS Nano*, 2015, **9**(9), 9380–9393.

33 P. Ramasamy, D.-H. Lim, B. Kim, S.-H. Lee, M.-S. Lee and J.-S. Lee, All-inorganic cesium lead halide perovskite nanocrystals for photodetector applications, *Chem. Commun.*, 2016, **52**(10), 2067–2070.

34 Z. Li, Q. Hu, Z. Tan, Y. Yang, M. Leng, X. Liu, C. Ge, G. Niu and J. Tang, Aqueous synthesis of lead halide perovskite nanocrystals with high water stability and bright photoluminescence, *ACS Appl. Mater. Interfaces*, 2018, **10**(50), 43915–43922.

35 F. Palazon, Q. A. Akkerman, M. Prato and L. Manna, X-ray lithography on perovskite nanocrystals films: from patterning with anion-exchange reactions to enhanced stability in air and water, *ACS Nano*, 2016, **10**(1), 1224–1230.

36 X. Zhang, X. Bai, H. Wu, X. Zhang, C. Sun, Y. Zhang, W. Zhang, W. Zheng, W. W. Yu and A. L. Rogach, Water-assisted size and shape control of CsPbBr3 perovskite nanocrystals, *Angew. Chem., Int. Ed.*, 2018, **57**(13), 3337–3342.

37 H. Huang, B. Chen, Z. Wang, T. F. Hung, A. S. Susha, H. Zhong and A. L. Rogach, Water resistant CsPbX 3 nanocrystals coated with polyhedral oligomeric silsesquioxane and their use as solid state luminophores in all-perovskite white light-emitting devices, *Chem. Sci.*, 2016, **7**(9), 5699–5703.

38 L. Wu, H. Hu, Y. Xu, S. Jiang, M. Chen, Q. Zhong, D. Yang, Q. Liu, Y. Zhao and B. Sun, From nonluminescent Cs4PbX6 (X= Cl, Br, I) nanocrystals to highly luminescent CsPbX3

 This journal is © The Royal Society of Chemistry 2026

Open Access Article. Published on 26 January 2026. Downloaded on 5/30/2026 3:48:49 AM. This article is licensed under a Creative Commons Attribution 3.0 Unported Licence.

nanocrystals: water-triggered transformation through a CsX-stripping mechanism, *Nano Lett.*, 2017, **17**(9), 5799–5804.

39 M. Crespo-Quesada, L. M. Pazos-Outón, J. Warnan, M. F. Kuehnel, R. H. Friend and E. Reisner, Metal-encapsulated organolead halide perovskite photocathode for solar-driven hydrogen evolution in water, *Nat. Commun.*, 2016, **7**(1), 12555.

40 M. Kim, J. H. Kim, M. Kim, C. S. Kim, J. W. Choi, K. Choi, J. H. Lee, J. Park, Y.-C. Kang and S.-H. Jin, Enhanced photoluminescence quantum efficiency and stability of water assisted CsPbBr3 perovskite nanocrystals, *J. Ind. Eng. Chem.*, 2020, **88**, 84–89.

41 W. Liu, J. Zheng, S. Cao, L. Wang, F. Gao, K.-C. Chou, X. Hou and W. Yang, General strategy for rapid production of low-dimensional all-inorganic CsPbBr3 perovskite nanocrystals with controlled dimensionalities and sizes, *Inorg. Chem.*, 2018, **57**(3), 1598–1603.

42 Y. Tong, E. Bladt, M. F. Aygüler, A. Manzi, K. Z. Milowska, V. A. Hintermayr, P. Docampo, S. Bals, A. S. Urban and L. Polavarapu, Highly luminescent cesium lead halide perovskite nanocrystals with tunable composition and thickness by ultrasonication, *Angew. Chem., Int. Ed.*, 2016, **55**(44), 13887–13892.

43 Z.-J. Li, E. Hofman, A. H. Davis, M. M. Maye and W. Zheng, General strategy for the growth of CsPbX3 (X= Cl, Br, I) perovskite nanosheets from the assembly of nanorods, *Chem. Mater.*, 2018, **30**(11), 3854–3860.

44 A. Jana, M. Mittal, A. Singla and S. Sapra, Solvent-free, mechanochemical syntheses of bulk trihalide perovskites and their nanoparticles, *Chem. Commun.*, 2017, **53**(21), 3046–3049.

45 H. Zamani, T.-H. Chiang, K. R. Klotz, A. J. Hsu and M. M. Maye, Tailoring CsPbBr3 Growth via Non-Polar Solvent Choice and Heating Methods, *Langmuir*, 2022, **38**(30), 9363–9371.

46 G. Xiang, Y. Zhou, W. Peng, J. Zhang, Y. Liu, J. Zhang, Z. Yue, X. Zhang, C. Song and B. Ding, Vacuum-deposited perovskite CsPbBr3 thin-films for temperature-stable Si based pure-green all-inorganic light-emitting diodes, *Ceram. Int.*, 2023, **49**(13), 21624–21633.

47 C. de Weerd, J. Lin, L. Gomez, Y. Fujiwara, K. Suenaga and T. Gregorkiewicz, Hybridization of single nanocrystals of Cs4PbBr6 and CsPbBr3, *J. Phys. Chem. C*, 2017, **121**(35), 19490–19496.

48 L. Rao, X. Ding, X. Du, G. Liang, Y. Tang, K. Tang and J. Z. Zhang, Ultrasonication-assisted synthesis of CsPbBr3 and Cs4PbBr6 perovskite nanocrystals and their reversible transformation, *Beilstein J. Nanotechnol.*, 2019, **10**(1), 666–676.

49 T. Xuan, S. Lou, J. Huang, L. Cao, X. Yang, H. Li and J. Wang, Monodisperse and brightly luminescent CsPbBr 3/Cs 4 PbBr 6 perovskite composite nanocrystals, *Nanoscale*, 2018, **10**(21), 9840–9844.

50 W. Sun, Y.-T. Hung, W.-T. Huang, R.-S. Liu and W. Zhou, Photoluminescent nano-CsPbBr3 embedded in Cs4PbBr6 crystals: formation mechanism and properties, *Cryst. Growth Des.*, 2023, **24**(1), 545–553.

51 J. Cao, X. Zeng, W. Li, L. Lv, C. Yan, H. Huang, J. Lu and W. Yang, Water-induced construction of Cs4PbBr6/CsPbBr3 heterojunction for efficient perovskite light-emitting diode, *Appl. Mater. Today*, 2023, **30**, 101733.

52 A. K. S. Kumar, Y. Zhang, D. Li and R. G. Compton, A mini-review: How reliable is the drop casting technique?, *Electrochem. Commun.*, 2020, **121**, 106867.

53 M. Abbas, L. Zeng, F. Guo, M. Rauf, X.-C. Yuan and B. Cai, A critical review on crystal growth techniques for scalable deposition of photovoltaic perovskite thin films, *Materials*, 2020, **13**(21), 4851.

54 X. Tang, N. L. Kothalawala, Y. Zhang, D. Qian, D. Y. Kim and F. Yang, Water-driven CsPbBr3 nanocrystals and poly (methyl methacrylate)-CsPbBr3 nanocrystal films with bending-endurable photoluminescence, *Chem. Eng. J.*, 2021, **425**, 131456.

55 F. Di Stasio, S. Christodoulou, N. Huo and G. Konstantatos, Near-unity photoluminescence quantum yield in CsPbBr3 nanocrystal solid-state films via postsynthesis treatment with lead bromide, *Chem. Mater.*, 2017, **29**(18), 7663–7667.

56 M. Liu, G. Zhong, Y. Yin, J. Miao, K. Li, C. Wang, X. Xu, C. Shen and H. Meng, Aluminum-doped cesium lead bromide perovskite nanocrystals with stable blue photoluminescence used for display backlight, *Adv. Sci.*, 2017, **4**(11), 1700335.

57 H. Zalrhi, M. Ouafi, M. Regragui, B. M. Soucase, F. Baig, Y. H. Khattak, U. Shafi, M. Abd-Lefdil and L. Atourki, Improving photoluminescence properties and reducing recombination of CsPbBr 3 perovskite through lithium doping, *RSC Adv.*, 2024, **14**(21), 15048–15057.

58 K.-C. Yeh and C.-H. Chan, High brightness and low operating voltage CsPbBr3 perovskite LEDs by single-source vapor deposition, *Sci. Rep.*, 2024, **14**(1), 3351.

59 D. Mao, L. Chen, Z. Sun, M. Zhang, Z.-Y. Shi, Y. Hu, L. Zhang, J. Wu, H. Dong and W. Xie, Observation of transition from superfluorescence to polariton condensation in CsPbBr3 quantum dots film, *Light: Sci. Appl.*, 2024, **13**(1), 34.

60 M. Van Der Laan, C. De Weerd, L. Poirier, O. Van De Water, D. Poonia, L. Gomez, S. Kinge, L. D. Siebbeles, A. F. Koenderink and T. Gregorkiewicz, Photon recycling in CsPbBr3 all-inorganic perovskite nanocrystals, *ACS Photonics*, 2021, **8**(11), 3201–3208.

61 S. Hu, X. Yan, Y. Zhang, B. Yang, H. Li and C. Sheng, Light-induced photoluminescence quenching and degradation in quasi 2D perovskites film of (C6H5C2H4NH3) 2 (CH3NH3) 2 [Pb3I10], *Appl. Sci.*, 2021, **11**(6), 2683.

62 H.-C. Chen, A. Shabir, C. M. Tan, P. Singh and J.-H. Lin, Degradation dynamics of quantum dots in white LED applications, *Sci. Rep.*, 2021, **11**(1), 24153.

63 H. Moon, C. Lee, W. Lee, J. Kim and H. Chae, Stability of quantum dots, quantum dot films, and quantum dot light-emitting diodes for display applications, *Adv. Mater.*, 2019, **31**(34), 1804294.

Open Access Article. Published on 26 January 2026. Downloaded on 5/30/2026 3:48:49 AM. This article is licensed under a Creative Commons Attribution 3.0 Unported Licence.

64 S. Huang, Z. Li, B. Wang, N. Zhu, C. Zhang, L. Kong, Q. Zhang, A. Shan and L. Li, Morphology evolution and degradation of CsPbBr3 nanocrystals under blue light-emitting diode illumination, *ACS Appl. Mater. Interfaces*, 2017, **9**(8), 7249–7258.

65 H. Chen, A. Guo, J. Zhu, L. Cheng and Q. Wang, Tunable photoluminescence of CsPbBr3 perovskite quantum dots for their physical research, *Appl. Surf. Sci.*, 2019, **465**, 656–664.

66 A. Dey, J. Ye, A. De, E. Debroye, S. K. Ha, E. Bladt, A. S. Kshirsagar, Z. Wang, J. Yin and Y. Wang, State of the art and prospects for halide perovskite nanocrystals, *ACS Nano*, 2021, **15**(7), 10775–10981.

67 P. Ijaz, M. Imran, M. M. Soares, H. l. C. Tolentino, B. Martín-García, C. Giannini, I. Moreels, L. Manna and R. Krahne, Composition-, size-, and surface functionalization-dependent optical properties of lead bromide perovskite nanocrystals, *J. Phys. Chem. Lett.*, 2020, **11**(6), 2079–2085.

68 K. H. Fausia, B. Nharangatt, R. N. Vinayakan, A. R. Ramesh, V. Santhi, K. R. Dhandapani, T. P. Manoj, R. Chatanathodi, D. Jose and K. Sandeep, Probing the Structural Degradation of CsPbBr3 Perovskite Nanocrystals in the Presence of H2O and H2S: How Weak Interactions and HSAB Matter, *ACS Omega*, 2024, **9**(7), 8417–8424.

69 D. Di Girolamo, M. I. Dar, D. Dini, L. Gontrani, R. Caminiti, A. Mattoni, M. Graetzel and S. Meloni, Dual effect of humidity on cesium lead bromide: enhancement and degradation of perovskite films, *J. Mater. Chem. A*, 2019, **7**(19), 12292–12302.

70 X. Liu and E.-C. Lee, Advancements in perovskite nanocrystal stability enhancement: a comprehensive review, *Nanomaterials*, 2023, **13**(11), 1707.

71 G. Annohene and G. Tepper, Moisture stability of perovskite solar cells processed in supercritical carbon dioxide, *Molecules*, 2021, **26**(24), 7570.

72 B. P. Kore, M. Jamshidi and J. M. Gardner, The impact of moisture on the stability and degradation of perovskites in solar cells, *Mater. Adv.*, 2024, **5**(6), 2200–2217.

73 A. Merdasa, M. Bag, Y. Tian, E. Kallman, A. Dobrovolsky and I. G. Scheblykin, Super-resolution luminescence microspectroscopy reveals the mechanism of photoinduced degradation in CH3NH3PbI3 perovskite nanocrystals, *J. Phys. Chem. C*, 2016, **120**(19), 10711–10719.

74 S. Meloni, G. Palermo, N. Ashari-Astani, M. Grätzel and U. Rothlisberger, Valence and conduction band tuning in halide perovskites for solar cell applications, *J. Mater. Chem. A*, 2016, **4**(41), 15997–16002.

75 M. R. Filip, G. E. Eperon, H. J. Snaith and F. Giustino, Steric engineering of metal-halide perovskites with tunable optical band gaps, *Nat. Commun.*, 2014, **5**(1), 5757.

76 L. Zhang, W. Geng, C.-j. Tong, X. Chen, T. Cao and M. Chen, Strain induced electronic structure variation in methyl-ammonium lead iodide perovskite, *Sci. Rep.*, 2018, **8**(1), 7760.

77 N. Phung, A. Mattoni, J. A. Smith, D. Skroblin, H. Köbler, L. Choubrac, J. Breternitz, J. Li, T. Unold and S. Schorr, Photoprotection in metal halide perovskites by ionic defect formation, *Joule*, 2022, **6**(9), 2152–2174.

78 E. V. Péan, S. Dimitrov, C. S. De Castro and M. L. Davies, Interpreting time-resolved photoluminescence of perovskite materials, *Phys. Chem. Chem. Phys.*, 2020, **22**(48), 28345–28358.

79 S. Singh, X. Wen and F. Yang, Effect of NaCl on the luminescent behavior of CsI thin films, *RSC Adv.*, 2025, **15**(44), 36993–37005.

80 S. Singh, X. Wen and F. Yang, Low temperature green synthesis of red emitting Pb-free $CsMnBr_3$ perovskite films, *Mater. Adv.*, 2026, DOI: 10.1039/D5MA01256B.

81 A. S. Abbas, D. Chabeda, D. Weinberg, D. T. Limmer, E. Rabani and A. P. Alivisatos, Non-Monotonic Size-Dependent Exciton Radiative Lifetime in $CsPbBr_3$ Nanocrystals, *Nat. Commun.*, 2025, **16**, 6401.

82 H. Fu and A. Zunger, InP quantum dots: Electronic structure, surface effects, and the redshifted emission, *Phys. Rev. B*, 1997, **56**(3), 1496.

83 Ü. Özgür, Y. I. Alivov, C. Liu, A. Teke, M. A. Reshchikov, S. Doğan, V. Avrutin, S.-J. Cho and H. Morkoc, A comprehensive review of ZnO materials and devices, *J. Appl. Phys.*, 2005, **98**(4), 041301.

84 T. Kirchartz, T. Markvart, U. Rau and D. A. Egger, Impact of small phonon energies on the charge-carrier lifetimes in metal-halide perovskites, *J. Phys. Chem. Lett.*, 2018, **9**(5), 939–946.

85 X. Tang, Y. Zhang, N. L. Kothalawala, X. Wen, D. Y. Kim and F. Yang, MAPbBr3 nanocrystals from aqueous solution for poly (methyl methacrylate)-MAPbBr3 nanocrystal films with compression-resistant photoluminescence, *Nanotechnology*, 2022, **33**(23), 235605.

86 S. Kahmann, O. Nazarenko, S. Shao, O. Hordiichuk, M. l. Kepenekian, J. Even, M. V. Kovalenko, G. R. Blake and M. A. Loi, Negative thermal quenching in FASnI3 perovskite single crystals and thin films, *ACS Energy Lett.*, 2020, **5**(8), 2512–2519.

87 Q. Zhang, M. He, Q. Wan, W. Zheng, M. Liu, C. Zhang, X. Liao, W. Zhan, L. Kong and X. Guo, Suppressing thermal quenching of lead halide perovskite nanocrystals by constructing a wide-bandgap surface layer for achieving thermally stable white light-emitting diodes, *Chem. Sci.*, 2022, **13**(13), 3719–3727.

88 S. Singh, X. Tang and F. Yang, Low-temperature synthesis of highly stable blue-emitting perovskite CsPbBr3 quantum dots, *J. Phys. Chem. C*, 2025, **129**(7), 3942–3950.

89 M. Mei, M. Kim, S. H. Park, G. E. Choi, S. Lee, R. A. Taylor, W. Chen, S. W. Hong and K. Kyhm, Comprehensive Analysis of Temperature-Dependent Photoluminescence in Silica-Encapsulated CsPbBr3 and CsPbI3 Perovskite Nanocrystals, *Nanomaterials*, 2026, **16**(1), 76.

90 M. Gerhard, B. Louis, R. Camacho, A. Merdasa, J. Li, A. Kiligaridis, A. Dobrovolsky, J. Hofkens and I. G. Scheblykin, Microscopic insight into non-radiative decay in perovskite semiconductors from temperature-dependent luminescence blinking, *Nat. Commun.*, 2019, **10**(1), 1698.

 This journal is © The Royal Society of Chemistry 2026

Open Access Article. Published on 26 January 2026. Downloaded on 5/30/2026 3:48:49 AM. This article is licensed under a Creative Commons Attribution 3.0 Unported Licence.

91 N. Shimosako, M. Kumamoto, Y. Muroga, Z. Liu, M. Sotome, T. Kondo, H. Kunugita and K. Ema, Exciton dynamics in $CsPbBr_3$ single crystal: LT splitting energy, exciton–polariton dispersion, and biexciton binding energy, *J. Chem. Phys.*, 2024, **161**(17), 174703.

92 X. T. Nguyen, K. Winte, D. Timmer, Y. Rakita, D. R. Ceratti, S. Aharon, M. S. Ramzan, C. Cocchi, M. Lorke and F. Jahnke, Phonon-driven intra-exciton Rabi oscillations in CsPbBr3 halide perovskites, *Nat. Commun.*, 2023, **14**(1), 1047.

93 D. R. Yakovlev, S. A. Crooker, M. A. Semina, J. Rautert, J. Mund, D. N. Dirin, M. V. Kovalenko and M. Bayer, Exciton–Polaritons in CsPbBr3 Crystals Revealed by Optical Reflectivity in High Magnetic Fields and Two-Photon Spectroscopy, *Phys. Status Solidi RRL*, 2024, **18**(3), 2300407.

94 A. M. Smith and S. Nie, Semiconductor nanocrystals: structure, properties, and band gap engineering, *Accounts Chem. Res.*, 2010, **43**(2), 190–200.

95 J. Li, X. Yuan, P. Jing, J. Li, M. Wei, J. Hua, J. Zhao and L. Tian, Temperature-dependent photoluminescence of inorganic perovskite nanocrystal films, *RSC Adv.*, 2016, **6**(82), 78311–78316.

96 M. C. Brennan, J. E. Herr, T. S. Nguyen-Beck, J. Zinna, S. Draguta, S. Rouvimov, J. Parkhill and M. Kuno, Origin of the size-dependent stokes shift in CsPbBr3 perovskite nanocrystals, *J. Am. Chem. Soc.*, 2017, **139**(35), 12201–12208.

97 S. B. Naghadeh, S. Sarang, A. Brewer, A. L. Allen, Y.-H. Chiu, Y.-J. Hsu, J.-Y. Wu, S. Ghosh and J. Z. Zhang, Size and temperature dependence of photoluminescence of hybrid perovskite nanocrystals, *J. Chem. Phys.*, 2019, **151**(15), 154705.

98 R. A. Scheidt, C. Atwell and P. V. Kamat, Tracking transformative transitions: From CsPbBr3 nanocrystals to bulk perovskite films, *ACS Mater. Lett.*, 2019, **1**(1), 8–13.

99 L. Protesescu, S. Yakunin, M. I. Bodnarchuk, F. Krieg, R. Caputo, C. H. Hendon, R. X. Yang, A. Walsh and M. V. Kovalenko, Nanocrystals of cesium lead halide perovskites (CsPbX3, X= Cl, Br, and I): novel optoelectronic materials showing bright emission with wide color gamut, *Nano Lett.*, 2015, **15**(6), 3692–3696.

100 J. Shi, M. Wang, Z. Da, C. Zhang, J. Wang, Y. Ding, Y. Xu and N. V. Gaponenko, Studies on the optical stability of CsPbBr 3 with different dimensions (0D, 1D, 2D, 3D) under thermal environments, *Nanoscale*, 2023, **15**(26), 11190–11198.

101 L. Gupta, S. Rath, S. Abbi and F. Jain, Temperature dependence of the fundamental band gap parameters in cadmium-rich Zn x Cd 1-x Se using photoluminescence spectroscopy, *Pramana*, 2003, **61**, 729–737.

102 P. Lautenschlager, M. Garriga, S. Logothetidis and M. Cardona, Interband critical points of GaAs and their temperature dependence, *Phys. Rev. B*, 1987, **35**(17), 9174.

103 Y.-L. Huang, W. Li and F. Yang, Eco-friendly synthesis and stability analysis of CsPbBr3 and poly (methyl methacrylate)-CsPbBr3 films, *Nanotechnology*, 2025, **36**(17), 175601.

104 B. Ai, C. Liu, Z. Deng, J. Wang, J. Han and X. Zhao, Low temperature photoluminescence properties of CsPbBr 3 quantum dots embedded in glasses, *Phys. Chem. Chem. Phys.*, 2017, **19**(26), 17349–17355.

105 E. V. Kulebyakina, M. L. Skorikov, E. V. Kolobkova, M. S. Kuznetsova, M. N. Bataev, D. R. Yakovlev and V. V. Belykh, Temperature-dependent photoluminescence dynamics of CsPbBr 3 and CsPb (Cl, Br) 3 perovskite nanocrystals in a glass matrix, *Phys. Rev. B*, 2024, **109**(23), 235301.

106 C. Xie, X. Li, J. Tong, Y. Gu and Y. Shen, Effects of white light-emitting diode (LED) light exposure with different Correlated Color Temperatures (CCT s) on human lens epithelial cells in culture, *Photochem. Photobiol.*, 2014, **90**(4), 853–859.

107 J. Lin, Y. Lu, X. Li, F. Huang, C. Yang, M. Liu, N. Jiang and D. Chen, Perovskite quantum dots glasses based backlit displays, *ACS Energy Lett.*, 2021, **6**(2), 519–528.

108 J. Lin, Z. Zhou, J. Lai, W. Ye, T. Pang, X. Li, L. Zeng, L. Lei, D. Yu and D. Chen, CsPbX3@ Glass (X= Cl, Br, I) Nanocomposites with Whole-Family High Absorption Efficiency above 75% for Backlit Display, *Laser Photon. Rev.*, 2025, **19**(4), 2401649.

109 Y. Lu, Y. Xu, S. Chen, J. Lin, J. Zhu, S. Wang, Y. Zheng, F. Huang and D. Chen, Ultra-narrowband emitting and highly stable CsPbX3@ glass@ PDMS (X3= Br3, Br1. 5I1. 5) monolithic composite film for backlit displays, *J. Lumin.*, 2022, **248**, 118952.

110 Y.-L. Tong, Y.-W. Zhang, K. Ma, R. Cheng, F. Wang and S. Chen, One-step synthesis of FA-directing FAPbBr3 perovskite nanocrystals toward high-performance display, *ACS Appl. Mater. Interfaces*, 2018, **10**(37), 31603–31609.

111 Y. Zu, J. Xi, L. Li, J. Dai, S. Wang, F. Yun, B. Jiao, H. Dong, X. Hou and Z. Wu, High-brightness and color-tunable FAPbBr3 perovskite nanocrystals 2.0 enable ultrapure green luminescence for achieving recommendation 2020 displays, *ACS Appl. Mater. Interfaces*, 2019, **12**(2), 2835–2841.

112 F. Zhang, J. Song, B. Han, T. Fang, J. Li and H. Zeng, High-Efficiency Pure-Color Inorganic Halide Perovskite Emitters for Ultrahigh-Definition Displays: Progress for Backlighting Displays and Electrically Driven Devices, *Small Methods*, 2018, **2**(10), 1700382.

113 H. C. Wang, S. Y. Lin, A. C. Tang, B. P. Singh, H. C. Tong, C. Y. Chen, Y. C. Lee, T. L. Tsai and R. S. Liu, Mesoporous silica particles integrated with all-inorganic CsPbBr3 perovskite quantum-dot nanocomposites (MP-PQDs) with high stability and wide color gamut used for backlight display, *Angew. Chem., Int. Ed.*, 2016, **55**(28), 7924–7929.

114 C. Sun, Y. Zhang, C. Ruan, C. Yin, X. Wang, Y. Wang and W. W. Yu, Efficient and stable white LEDs with silica-coated inorganic perovskite quantum dots, *Adv. Mater.*, 2016, **28**(45), 10088–10094.

115 X. Zhang, H.-C. Wang, A.-C. Tang, S.-Y. Lin, H.-C. Tong, C.-Y. Chen, Y.-C. Lee, T.-L. Tsai and R.-S. Liu, Robust and stable narrow-band green emitter: an option for advanced

Open Access Article. Published on 26 January 2026. Downloaded on 5/30/2026 3:48:49 AM.
This article is licensed under a Creative Commons Attribution 3.0 Unported Licence.

wide-color-gamut backlight display, *Chem. Mater.*, 2016, **28**(23), 8493–8497.

116 K. Ma, X.-Y. Du, Y.-W. Zhang and S. Chen, In situ fabrication of halide perovskite nanocrystals embedded in polymer composites via microfluidic spinning microreactors, *J. Phys. Chem. C*, 2017, **5**(36), 9398–9404.

117 J. Y. Sun, F. T. Rabouw, X. F. Yang, X. Y. Huang, X. P. Jing, S. Ye and Q. Y. Zhang, Facile two-step synthesis of all-inorganic perovskite CsPbX3 (X= Cl, Br, and I) zeolite-Y composite phosphors for potential backlight display application, *Adv. Funct. Mater.*, 2017, **27**(45), 1704371.

118 S. M. Qaid, H. M. Ghaithan, B. A. Al-Asbahi, A. Alqasem and A. S. Aldwayyan, Fabrication of thin films from powdered cesium lead bromide (CsPbBr3) perovskite quantum dots for coherent green light emission, *ACS Omega*, 2020, **5**(46), 30111–30122.

119 M. He, C. Wang, J. Li, J. Wu, S. Zhang, H.-C. Kuo, L. Shao, S. Zhao, J. Zhang and F. Kang, CsPbBr 3–Cs 4 PbBr 6 composite nanocrystals for highly efficient pure green light emission, *Nanoscale*, 2019, **11**(47), 22899–22906.

 This journal is © The Royal Society of Chemistry 2026